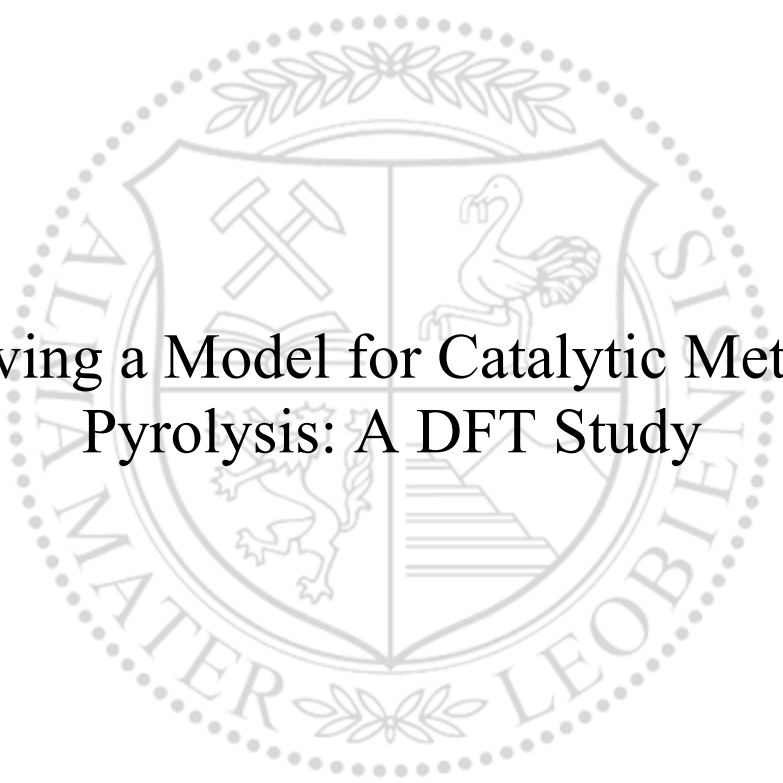




Chair of Physical Metallurgy

Master's Thesis



Deriving a Model for Catalytic Methane  
Pyrolysis: A DFT Study

Ulrich Josef Pototschnig, BSc

February 2023





**EIDESSTÄTLICHE ERKLÄRUNG**

Ich erkläre an Eides statt, dass ich diese Arbeit selbständig verfasst, andere als die angegebenen Quellen und Hilfsmittel nicht benutzt, und mich auch sonst keiner unerlaubten Hilfsmittel bedient habe.

Ich erkläre, dass ich die Richtlinien des Senats der Montanuniversität Leoben zu "Gute wissenschaftliche Praxis" gelesen, verstanden und befolgt habe.

Weiters erkläre ich, dass die elektronische und gedruckte Version der eingereichten wissenschaftlichen Abschlussarbeit formal und inhaltlich identisch sind.

Datum 14.02.2023

---

Unterschrift Verfasser/in  
Ulrich Josef Pototschnig



---

# Acknowledgements

Completing a master's thesis requires the assistance and patience of many people, and I am very grateful to have been granted with both. First, I want to express my deepest gratitude to my supervisor Dr. David Holec for his constant support, ingenuity, supervision and trust during the last three years that I have been working in the CMS group.

I want to thank Dominik Gehringer, who was always available for help and shared much of his wealth of experience with me. I also thank all my colleagues from the CMS Group, with whom I have always been enjoying working together. Furthermore, I would like to thank David Scheiblehner, Prof. Helmut Antrekowitsch and the Chair of Nonferrous Metallurgy for granting me detailed insights into the practical side of the project. The computational results presented have been achieved using the Vienna Scientific Cluster (VSC) and the Montanuniversität Leoben High Performance Computing Cluster (MUL-HPC).

I would also like to thank my friends (Johann, Matthias, Max, Michael and Zenad) for their constant support, but especially for the distraction they have provided in the most positive sense throughout the years. In closing, I would like to thank my family. I am deeply grateful to my parents for giving me the courage and, above all, the opportunity to do what I want to do. Without their permanent moral and financial support, this work would never have been possible. And finally my sister, who was and always will be my greatest role model.



---

# Contents

<b>Contents</b>	<b>vii</b>
<b>Abstract</b>	<b>1</b>
<b>Zusammenfassung</b>	<b>3</b>
<b>1 Introduction</b>	<b>5</b>
1.1 Hydrogen . . . . .	5
1.1.1 Methane pyrolysis . . . . .	6
1.2 Heterogeneous catalysis . . . . .	6
1.2.1 Adsorption . . . . .	7
1.2.2 Sabatier principle . . . . .	7
1.2.3 Transition-state theory . . . . .	8
1.2.4 Potential energy surfaces . . . . .	10
1.2.5 Adsorption energy trends . . . . .	11
1.2.6 Rate constants . . . . .	12
1.2.7 Reaction rates . . . . .	13
1.2.8 Microkinetic model . . . . .	13
1.3 Methane pyrolysis . . . . .	16
<b>2 Methodology</b>	<b>21</b>
2.1 Density Functional Theory . . . . .	21

2.1.1	Hohenberg-Kohn theorems . . . . .	22
2.1.2	Kohn-Sham equations . . . . .	22
2.2	VASP . . . . .	24
2.2.1	INCAR . . . . .	24
2.2.2	KPOINTS . . . . .	26
2.2.3	POSCAR . . . . .	26
2.2.4	POTCAR . . . . .	26
2.3	Approach . . . . .	27
2.3.1	Molecular energies . . . . .	27
2.3.2	Adsorption energies . . . . .	27
2.3.3	PES calculations . . . . .	29
2.3.4	Nudged elastic band calculations . . . . .	30
<b>3</b>	<b>Results</b>	<b>31</b>
3.1	Model input calculations . . . . .	31
3.1.1	Molecular energies . . . . .	31
3.1.2	Adsorption energy trends . . . . .	32
3.1.3	Chemical correlations . . . . .	35
3.1.4	PES . . . . .	36
3.1.5	Free site coverage $\theta_*$ . . . . .	38
3.1.6	Activation energy . . . . .	39
3.2	Reaction rate . . . . .	40
3.3	Limitations . . . . .	45
3.3.1	Molecule orientation . . . . .	45
3.3.2	Surface geometry and composition . . . . .	46
3.3.3	Linearity . . . . .	47
3.3.4	Carbon . . . . .	47
3.3.5	Entropy . . . . .	47



3.3.6	Rate-determining step . . . . .	47
3.3.7	Computational accuracy . . . . .	47
<b>4</b>	<b>Conclusions</b>	<b>49</b>
	<b>Bibliography</b>	<b>51</b>



---

# Abstract

Hydrogen is an essential commodity in any industrialized society, and its importance will continue to increase with current efforts to decarbonize the industrial and transportation sector. While conventional hydrogen production itself causes greenhouse gas emissions, methane pyrolysis provides a scalable alternative. However, operating temperatures above 1300 K are too high for industrial hydrogen production via methane pyrolysis. Thus, a major scientific goal is to find a catalyst material that lowers operating temperatures, making methane pyrolysis economically viable.

In this work, we derive a model that provides qualitative comparison of possible catalyst materials. The model is largely based on calculations of adsorption energies using density functional theory. Thirty different elements were considered. Results show that adsorption energies of intermediate molecules in the methane pyrolysis reaction correlate linearly with the adsorption energy of carbon. Moreover, the adsorption energy increases with decreasing group number in the d-block of the periodic table.

For a temperature range between 600 and 1200 K and a normalized partial pressure range for  $\text{H}_2$  between  $10^{-1}$  and  $10^{-5}$ , a total of seventeen different materials were found to be optimal catalysts at least once. This indicates that catalyst selection and reactor operating conditions should be well matched. The present work establishes the foundation for future large-scale studies of surfaces, alloy compositions, and material classes using machine learning algorithms.



---

# Zusammenfassung

Wasserstoff ist ein wesentlicher Rohstoff einer jeden Industriegesellschaft und seine Bedeutung wird mit den derzeitigen Bemühungen um die Dekarbonisierung des Industrie- und Transportsektors noch weiter zunehmen. Während die konventionelle Wasserstoffproduktion selbst Treibhausgasemissionen verursacht, bietet die Methanpyrolyse eine vielversprechende Alternative. Allerdings sind die Betriebstemperaturen über 1300 K angesiedelt und somit für eine wirtschaftliche Wasserstoffproduktion zu hoch. Ein wichtiges Forschungsziel ist es daher, ein Katalysatormaterial zu finden, welches die Betriebstemperaturen signifikant herabsenkt, um so eine Wasserstoffproduktion mittels Methanpyrolyse auf industriellem Maßstab zu ermöglichen.

In dieser Arbeit leiten wir ein Modell ab, das einen qualitativen Vergleich von möglichen Katalysatormaterialien erlaubt. Das Modell basiert weitgehend auf Berechnungen von Adsorptionsenergien unter Verwendung der Dichtefunktionaltheorie. Dreißig verschiedene Elemente wurden berücksichtigt. Die Ergebnisse zeigen, dass die Adsorptionsenergien der Zwischenprodukte während der Methanpyrolysereaktion linear mit der Adsorptionsenergie von Kohlenstoff korrelieren. Außerdem steigt die Adsorptionsenergie mit abnehmender Gruppennummer im d-Block des Periodensystems.

Für einen Temperaturbereich zwischen 600 und 1200 K und einen normalisierten Partialdruckbereich von  $\text{H}_2$  zwischen  $10^{-1}$  und  $10^{-5}$  erwiesen sich insgesamt siebzehn verschiedene Materialien mindestens einmal als optimale Katalysatoren. Dies zeigt, dass die Auswahl des Katalysators und die Betriebsbedingungen des Reaktors gut aufeinander abgestimmt sein sollten. Die vorliegende Arbeit bildet die Grundlage für künftige Untersuchungen von Oberflächen, Legierungszusammensetzungen und Materialklassen unter Verwendung von Algorithmen des maschinellen Lernens.



---

# Introduction

Climate change refers to long-term shifts in temperatures and weather patterns. It is caused by emission of greenhouse gases such as carbon dioxide ( $\text{CO}_2$ ), nitrogen dioxide ( $\text{NO}_2$ ) or methane ( $\text{CH}_4$ ) [1]. Since the 19th century, human-based activity has been the main source of these emissions. Greenhouse gas concentrations in Earth's atmosphere have reached their highest levels in 800,000 years, causing major changes in sea levels, biodiversity, agriculture, and many other aspects of life on the Earth [2].

In order to stop this development, the European Commission has presented a number of policy initiatives, the so-called "Green New Deal". The goal is to reach net-zero carbon dioxide emissions in the European Union by 2050 [3]. A major cornerstone of this policy is a massive expansion of hydrogen-based technologies in industry and transportation to replace traditional fossil-carbon based energy sources [4]. This process will require a massive increase in hydrogen production.

## 1.1 Hydrogen

Hydrogen is the lightest element and forms a gaseous diatomic molecule  $\text{H}_2$  at standard conditions [5]. Hydrogen production technologies are divided into different categories based on their environmental impact. There are three main categories [6]:

- **Grey hydrogen** is hydrogen produced from non-renewable resources such as natural gas and coal, causing  $\text{CO}_2$  emissions during the production process. The main process is steam methane reforming. Grey hydrogen currently accounts for roughly 98% of global hydrogen production [7].
- **Turquoise hydrogen** is carbon-free, even though it is dependent on non-renewable resources. In contrast to other technologies, turquoise hydrogen technologies, such as methane pyrolysis, are still in development.

- **Green hydrogen** is produced using renewable electricity. The most widely used technology is water electrolysis with a share of 2% of global hydrogen production [7].

At first glance, green hydrogen seems to be the most environmentally friendly option. However, power consumption during water electrolysis is high: Assuming 100% efficiency, an electrolyser would consume 39.4 kWh/kg H<sub>2</sub> [8]. Current electrolysers achieve 70% efficiency [9], resulting in roughly 55 kWh/kg H<sub>2</sub>. Electricity prices for non-household consumers have been as high as 0.14€/kWh in Austria in the first half-year of 2022 [10] resulting in a price of 7.7€/kg H<sub>2</sub>. Grey hydrogen production from steam methane reforming with subsequent carbon capture and storage costs 1.3€/kg H<sub>2</sub> [11], reducing costs by almost a factor of 6. Moreover, this calculation is based on the assumption that only electricity from renewable energy sources is used, which does not reflect the current Austrian or European electricity mix. Thus, hydrogen produced by an electrolysis process is presently not emission-free.

### 1.1.1 Methane pyrolysis

Until Europe will have fully converted its power generation to renewable sources, which is still decades away, a bridging hydrogen production technology which is economically and ecologically viable will be required. A promising option is methane pyrolysis. Methane pyrolysis is the thermal decomposition of methane in the absence of oxygen to form solid carbon and hydrogen. Although CO<sub>2</sub> emission-free, methane needs to be obtained from natural gas, making it a turquoise hydrogen technology. Nevertheless, since natural gas is a cheap and abundant commodity on Earth, pyrolysis could serve as an ideal bridging candidate. From an energetic point of view, only 37.5 kJ of energy is necessary to produce 1 mol of H<sub>2</sub> in the process of methane pyrolysis, compared to 286 kJ required for water electrolysis [12]. At present, however, the technology has not yet reached market maturity. For reasonable conversion rates, operating temperatures are around 1050°C and therefore unprofitable [13]. This could be solved by a catalyst that allows for lower temperatures, making the process available for large-scale hydrogen production.

The aim of this work is to qualitatively investigate possible catalyst materials for methane pyrolysis using computational methods. However, before such a computational model can be presented, fundamentals of heterogeneous catalysis are required.

## 1.2 Heterogeneous catalysis

The following sections attempt to answer three general questions of catalysis and derive a framework that is subsequently applied to methane pyrolysis in particular:



- What property makes a material catalytic?
- How to describe complex catalytic reactions?
- How can computational methods be used to obtain qualitative trends?

As a main concept, the Sabatier principle will be discussed, which is a qualitative approach to explain heterogeneous catalysis [14]. First of all, as a prerequisite to understand the work of Sabatier, important properties of catalysts, such as the phenomenon of adsorption are elaborated.

### 1.2.1 Adsorption

In catalysis, the most important process is adsorption, which is the attachment of atoms or molecules to a solid surface. Desorption is the reverse process. The substance that adsorbs is called the adsorbate and the material to which it adsorbs is called substrate [15]. Hence, the substrate represents the catalyst.

Two types of adsorption are distinguished: Physisorption and chemisorption. While physisorption involves van der Waals interactions, chemisorption results in the formation of a chemical bond between the adsorbent and the substrate. Therefore, chemisorption leads to stronger bonds and the interatomic distances are shorter [15]. Since chemisorption is more relevant for catalysis than physisorption, from this point on the term chemisorption will be replaced by adsorption.

The adsorption energy,  $\Delta E_{\text{Ads}}$ , of an adsorbed atom/molecule is the energy that has to be delivered to the adsorbed atom/molecule to be desorbed from a substrate surface [16]. Intuitively, adsorption energies do not only change for different adsorbates, but also for different substrate elements and surface sites, which allows specific substrates to act as catalysts.

### 1.2.2 Sabatier principle

In general, adsorption promotes non-equilibrated chemical reactions. The stronger the adsorption, i.e., the more negative  $\Delta E_{\text{Ads}}$ , the higher the reaction rate constant  $k$  becomes which reflects the speed of a reaction in a specific direction. For the time being, it is only important that higher adsorption energies correlate with higher reaction rates. The concept of non-equilibrium chemical reactions will be discussed later.

With increasing magnitude for negative  $\Delta E_{\text{Ads}}$  values, reactants or products are adsorbed more strongly to the substrate. More energy is required for products to desorb from the surface, resulting in a lack of free surface sites, which is denoted as a fraction of total

surface sites and has the symbol  $\theta_*$ . This is called catalyst deactivation. In such a case, the only options are either a replacement of the catalyst material or a reactivation, which is unfavourable because it would require halting the production operation [17]. Conversely, a very low adsorption energy corresponds to weak catalytic activity. Thus, the reaction rather resembles a reaction in absence of a catalyst.

These two concurring mechanisms caused by adsorption are responsible for the characteristic volcano-shaped plots of catalytic reaction rates  $R$ , as shown in Fig. 1.1 [18]. In the upper plot, logarithm of the reaction rate constant  $k_1$  and fraction of free surface sites  $\theta_*$  for a fictitious reaction are plotted as a function of  $\Delta E_{\text{Ads}}$ . The combination of both lines is seen in the bottom graph. The reaction rate  $R$  increases with decreasing adsorption energies ( $k_1 \rightarrow \infty$ ) until a maximum is reached where the lack of free surface sites is starting to limit the process ( $\theta_* \rightarrow 0$ ). The task is to find a catalyst material with an adsorption energy as close as possible to this maximum. In other words, interactions between a reactant and an ideal catalyst are neither too strong nor too weak. This is called the Sabatier principle [19].

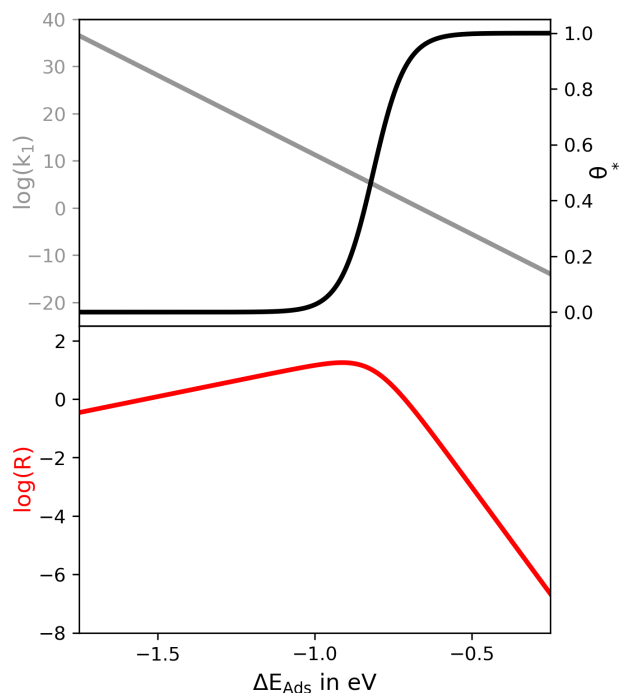


Figure 1.1: Top: Coverage of free sites,  $\theta_*$  (black) and logarithm of the forward rate,  $\log(k_1)$  (grey), as a function of  $\Delta E_{\text{Ads}}$ . Bottom: Logarithm of the reaction rate  $R$  as a function of  $\Delta E_{\text{Ads}}$ .

Since reaction rates easily span many orders of magnitude, the description of complex chemical processes in their entirety is difficult. This is the reason why Sabatier analysis does not yield quantitative values, even though the reaction rate  $R$  possesses a frequency unit of  $\text{s}^{-1}$  per surface site. Nevertheless, this does not affect the capability of volcano plots as a qualitative comparison tool for different catalyst materials.

To better understand the influence of a catalyst on a chemical reaction, the next chapter will discuss chemical reactions from an energetic point of view and expand on the role of adsorption during a catalytic reaction.

### 1.2.3 Transition-state theory

One of the most profound relationships in physical chemistry is Hess's law, which states that the change in enthalpy during a chemical reaction is path independent [20]. Enthalpy is a property of a thermodynamic system and is the sum of the internal energy  $U$  of the system

and the product of its volume  $V$  and pressure  $p$  [15]:

$$H = U + pV. \quad (1.1)$$

Hess's law allows the calculation of the change in enthalpy during a chemical reaction as

$$\Delta H_{\text{Reaction}}^{\circ} = \sum \nu_{\text{p}} \Delta H_{\text{f}(\text{p})}^{\circ} - \sum \nu_{\text{r}} \Delta H_{\text{f}(\text{r})}^{\circ}, \quad (1.2)$$

where  $\Delta H_{\text{f}(\text{p})}^{\circ}$  and  $\Delta H_{\text{f}(\text{r})}^{\circ}$  are enthalpies of formation of products and reactants with their respective stoichiometric coefficients,  $\nu_{\text{p}}$  and  $\nu_{\text{r}}$ , which denote how many molecules are involved in the chemical reaction. Enthalpy is usually expressed in J/mol. Since this work covers a model that calculates individual atomic bonds, a change from enthalpy  $H$  in J/mol to potential energy  $E$  in eV/particle is reasonable, despite the fact that it is only an approximation, since it neglects the  $pV$  term, which is a component of  $U$ . For the consideration of atomic phenomena, however, this simplification is useful and makes it possible to rewrite Hess's law as

$$\Delta E_{\text{Reaction}}^{\circ} = \sum \nu_{\text{p}} \Delta E_{(\text{p})}^{\circ} - \sum \nu_{\text{r}} \Delta E_{(\text{r})}^{\circ}, \quad (1.3)$$

with  $\Delta E_{(\text{p})}^{\circ}$  and  $\Delta E_{(\text{r})}^{\circ}$  as potential energies of products and reactants, respectively.

Although the net energy change in a chemical reaction is path-independent, the change in potential energy does not necessarily correspond to the energy change during the reaction. Fig. 1.2 shows the potential energy over a reaction coordinate for a hypothetical chemical reaction. This type of diagram is also known as a potential energy diagram (PED). The reaction coordinate represents atomic displacements, e.g. interatomic distances, which are directly involved in the formation of products, thus it represents the progress of a reaction [15].

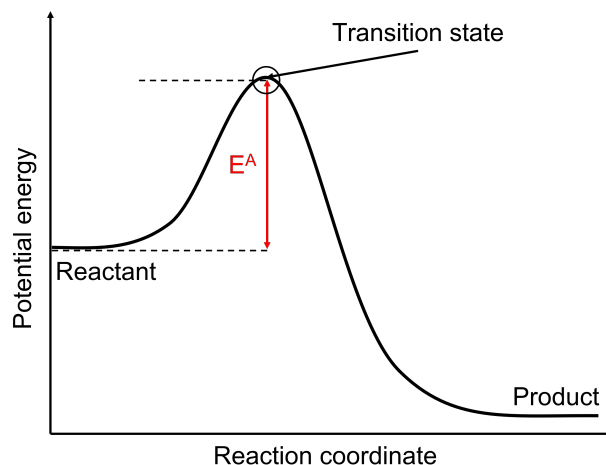


Figure 1.2: Potential energy diagram (PED) for a hypothetical reaction.

Potential energy reaches a maximum at the so-called transition state. The required energy to reach this maximum is called activation energy  $E^A$ . Since a complete derivation of

transition-state theory would go beyond the scope of this thesis, a well-elaborated description is provided in chapter 4 of [14]. In essence, the concept of a transition state can link statistical thermodynamics and the reaction rate constant  $k$ , that was already mentioned in chapter 1.2.2, where  $k$  indicates the tendency for a reaction to proceed in a certain direction. The activation energy  $E_A$ , which represents the difference in potential energy between the reactant state and the transition state, is connected to the rate constant  $k$  of an elementary reaction via

$$k = \frac{k_B T}{h} \exp\left(\frac{-\Delta G_{TS}^\circ}{k_B T}\right) \quad (1.4)$$

with

$$\Delta G_{TS}^\circ = E^A - T\Delta S_{TS}^\circ, \quad (1.5)$$

where  $k_B$  is the Boltzmann constant,  $T$  the temperature,  $h$  the Planck constant,  $\Delta G_{TS}^\circ$  the standard Gibbs free energy of the transition state and  $\Delta S_{TS}^\circ$  the standard entropy of the transition state.

### 1.2.4 Potential energy surfaces

In chapter 1.2.2 it was also noted that a catalyst promotes non-equilibrium chemical reactions and that adsorption determines this effect. This allows for a refinement of  $E^A$  by adding that a catalyst changes the magnitude of  $E^A$ , and therefore changing the reaction rate [21]. Reasons for this phenomenon will be discussed in the next chapter. At this point, the important conclusion to be drawn is that the potential energy for a chemical energy, where a catalyst is present, is no longer only a function of the reaction coordinate, but also a function of the distance between the molecule and a catalytic surface.

It should be noted that the reaction coordinate itself is usually a multidimensional vector containing all atomic coordinates. Therefore, the reaction coordinate is simplified to the distance between the dissociating H atom and the central C atom. Similarly, the introduction of a catalyst surface leads to the reaction depending not only on the distance to the nearest catalyst surface atom, but also on every other surface atom and the respective orientation between the molecule and the surface. These factors are neglected to simplify the model.

This second coordinate necessitates the use of a two-dimensional potential energy diagram for catalytic reactions, also known as a potential energy surface (PES). In Fig. 1.3, the PES for a dissociation reaction of a CH molecule is depicted as a function of its distance from a (111) fcc-Al surface. Every horizontal line on the PES represents a PED as shown in Fig. 1.2 for a specific distance between substrate and adsorbate. The three-dimensional rendering of the PES clarifies the role of a catalytic surface by clearly illustrating the decrease in energy for a given reaction.

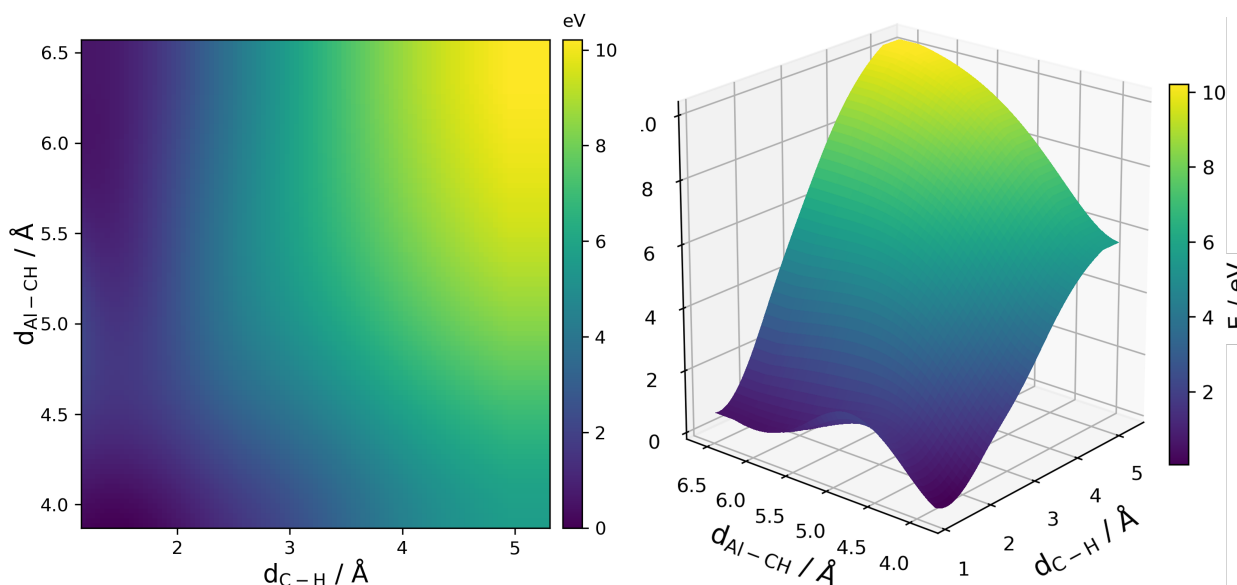


Figure 1.3: Exemplary potential energy surface (PES) for a dissociation of CH on a (111) Al surface.

Potential energy surfaces such as Fig. 1.3 can be calculated using computational methods that will be described in chapter 2.3.3. However, these calculations are computationally very demanding and have to be carried out for every single chemical reaction step on every surface. For instance, decomposition of methane consists of four dissociation steps where the central C atom loses an H atom during every step, resulting in four PES calculations for only one catalyst surface. Hence, such calculations are not suitable for extensive catalyst material screening. Luckily, adsorption energies show specific trends that help to reduce computational effort. These trends will be discussed in the next chapter.

## 1.2.5 Adsorption energy trends

In general, adsorption energies of molecules that bind to the surface through the same element(s) scale with each other for different substrates. This is especially true for methane, for which the scaling behaves linearly with respect to carbon [22]. Thus, the adsorption energy scaling relation  $\Delta E_{\text{CH}_n}$  for a molecule  $\text{CH}_n$  can be approximated as

$$\Delta E_{\text{Ads,CH}_n} = \gamma(n)\Delta E_{\text{Ads,C}} + \xi, \quad (1.6)$$

with  $\gamma(n)$  as a surface-independent scaling slope,  $\Delta E_{\text{Ads,C}}$  as the adsorption energy of carbon and  $\xi$  as a constant. The main achievement of this relationship is that once scaling parameters for a molecule are determined and the adsorption energy of carbon is calculated for one of the examined systems, the adsorption energy equation is expressed as a function of only  $\Delta E_{\text{Ads,C}}$ .

Since adsorption energies and activation energies are governed by the same fundamental physics, their correlation is a plausible consequence [14]. In general, assuming a set of

elements  $i$  with corresponding adsorption energies  $\Delta E_{\text{Ads},i}$ , the activation energy can be defined as

$$E^{\text{A}} = \sum_{i=1}^N \gamma_i \Delta E_{\text{Ads},i} + \xi. \quad (1.7)$$

In the case of methane, the set of adsorption energies exclusively consists of  $\Delta E_{\text{Ads},\text{C}}$ , as has been shown by Abild-Pedersen et al. [22]. Similarly, a connection to the reaction energy can be written as

$$\Delta E = \sum_{i=1}^N (\Delta \gamma_i \Delta E_{\text{Ads},i}) + \Delta \xi. \quad (1.8)$$

In contrast, the reaction energy is dependent on the change in scaling slope,  $\Delta \gamma_i$ , where the sum covers all atoms  $i$  that form a bond to the surface. This change in scaling slope is calculated from the slopes in linear adsorption scaling relations.  $\Delta E_{\text{Ads},i}$  denotes the binding energy of relevant base elements, i.e.,  $\Delta E_{\text{Ads},\text{C}}$ . The change in the  $\xi$  parameter,  $\Delta \xi$ , must be calculated once using the change in reaction energy for a catalyst surface that is part of the adsorption energy relation [22], i.e., a PES calculation has to be carried out for one single system. Here, the main advantage of adsorption energy scaling relations becomes evident: Only one PES calculation per reaction step is necessary to determine catalytic activity of any substrate material as long as the PES substrate is part of the adsorption energy trend.

In this context, it should be mentioned that linearity of adsorption energy relations is not a necessary prerequisite. Thus, virtually all functional relations are applicable to this model, however, leading to a significant complication regarding its implementation. Since methane and its intermediates show a linear correlation for many different structures, a linear relation will be used for the complete model derivation in chapter 1.3.

The reaction rate  $R$  cannot be determined from the reaction energies alone. Instead, a deeper understanding of the reaction rate itself and a model to handle complex multistep reactions is required.

### 1.2.6 Rate constants

Consider a simple exemplary chemical reaction of a gaseous reactant  $A$  that is forming a gaseous product  $B$ . Upon equilibrium the reaction can be formulated as



Here,  $k_1$  and  $k_{-1}$  are rate constants for the forward and backward reaction, respectively. Rate constants represent the speed of the reaction in a specific direction. In equilibrium, the relation between  $k_1$  and  $k_{-1}$  is constant, allowing a definition of an equilibrium constant  $K_1$

as

$$K_1 = \frac{k_1}{k_{-1}} = \frac{p_B}{p_A} = \exp\left(\frac{-\Delta G_1^\circ}{k_B T}\right), \quad (1.10)$$

with partial pressures  $p_A$  and  $p_B$  of species A and B, respectively, the Boltzmann constant  $k_B$ , the temperature  $T$ , and the standard Gibbs energy of reaction  $\Delta G_1^\circ$  as

$$\Delta G_1^\circ = \Delta E_1 - T\Delta S_1 \quad (1.11)$$

where  $\Delta E_1$  is the reaction energy and  $\Delta S_1$  the change in entropy. Eq. (1.10) is also known as the law of mass action [23]. Importantly, the difference to Eqs. (1.4) and (1.5), respectively, has to be noted. Those described the transition state and thus focused on the expenditure of a reaction to occur, whereas the equilibrium constant depends solely on the net energy difference between reactants and products.

### 1.2.7 Reaction rates

The difficulty in describing catalytic reactions, however, is that they are *not* in equilibrium and therefore *not* constant. Thus, non-equilibrated chemical reactions are described by so-called reaction rates. A reaction rate  $R$  is the net speed at which a reaction takes place [24]. Hence, the goal of a catalyst is to increase the speed of a reaction in a desired direction. However, a catalyst can only enhance the rate of a thermodynamically feasible reaction but cannot change the thermodynamic equilibrium itself [17].

In general, common heterogeneous catalytic reactions consist of many reaction steps which lead to a reaction rate expression that is a function of many different parameters such as temperature  $T$ , partial pressures  $p_i$ , rate constants  $k_i$  and equilibrium constants  $K_i$ , and the chemical activity of the catalyst itself [25]:

$$R = f(\text{catalyst}, T, p_i, \dots, k_i, \dots, K_i, \dots). \quad (1.12)$$

Therefore, it is important to divide a reaction into its elementary steps and treat every step separately. This breakdown is accomplished with a microkinetic model.

### 1.2.8 Microkinetic model

Microkinetic modeling provides the framework for the analysis of reaction mechanisms and yields valuable information about rate-limiting reactions. A general strategy for the formulation of a microkinetic model is to develop a reaction scheme that comprises all elemental surface events that occur during the catalytic conversion of reactants to products, including all relevant intermediates [26]. Therefore, Eq. (1.9) is considered again, however, in this

configuration the equation undergoes a heterogeneous catalytic reaction as illustrated in Fig. 1.4.

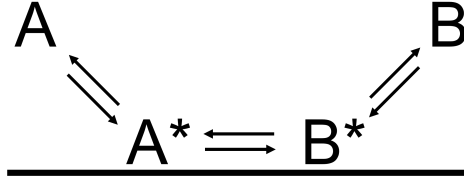


Figure 1.4: Schematic representation of a simple heterogeneous catalytic reaction.

Three elementary steps are distinguished: Reactant A is adsorbed on a catalyst surface site (1.13), which is denoted by a superscript \*. This adsorbed reactant reacts to form adsorbed product B\* (1.14), which subsequently desorbs in order to make its surface site available for another reaction (1.15). Instead of a single reaction step, three reaction steps must be defined.



Assuming there are N active sites available, three reaction rate expressions are derived:

$$R_1 = k_1 p_A N \theta_* - k_{-1} N \theta_A \quad (1.16)$$

$$R_2 = k_2 N \theta_A - k_{-2} N \theta_B \quad (1.17)$$

$$R_3 = k_3 N \theta_B - p_B k_{-3} N \theta_* \quad (1.18)$$

$\theta_A$ ,  $\theta_B$  and  $\theta_*$  represent the coverage of A species, B species and free sites, respectively, which are always numbers between 0 and 1. Thus, the term  $N\theta_*$  refers to the total number of free surface sites where a catalytic reaction can take place.

This results in two options to solve this system of linear equations. One option is to assume steady-state conditions where the time-derivatives of the coverages are 0, i.e.,

$$\frac{d\theta_A}{dt} = \frac{d\theta_B}{dt} = 0. \quad (1.19)$$

Including the site-conservation rule, which states that there are no other species present, it follows that

$$\theta_A + \theta_B + \theta_* = 1, \quad (1.20)$$



and a rate expression  $R$  can be derived which treats all three reaction steps as if they are proceeding with the same rate.

In reality, however, systems exist that A) require more elementary steps to describe a reaction, which leads to a more complex derivation of  $R$ , and B) have elementary steps that do not contribute equally to the overall reaction rate. Thus, an alternative approach is to define a rate-determining step. A rate-determining step is an elementary step that determines the overall reaction rate, i.e., a step that acts as a “kinetic bottleneck”. This is also called quasi-equilibrium, since equilibrium constants are thereby assigned to each reaction step except for the rate-determining step [25]. In the case of catalytic methane pyrolysis, this quasi-equilibrium approach is more appropriate. Albeit, a derivation for this simpler schematic catalytic reaction from Fig. 1.4 is given.

Assuming reaction step (1.14) is rate-determining, equilibrium constants are defined for (1.13) and (1.15) which results in surface coverages  $\theta_A$  and  $\theta_B$  of

$$K_1 = \frac{k_1}{k_{-1}} = \frac{N\theta_A}{p_A N\theta_*} \rightarrow \theta_A = K_1 p_A \theta_*, \quad (1.21)$$

and

$$K_3 = \frac{k_3}{k_{-3}} = \frac{p_B N\theta_*}{N\theta_B} \rightarrow \theta_B = \frac{p_B \theta_*}{K_3}. \quad (1.22)$$

The last unknown variable,  $\theta_*$ , can be solved with the site conservation rule from (1.20), resulting in

$$\theta_* = \frac{1}{1 + K_1 p_A + \frac{p_B}{K_3}}. \quad (1.23)$$

It is not possible to define an equilibrium constant for (1.14). However, it is convenient to define an “approach to equilibrium”  $\gamma$  [14]. This approach to equilibrium is a positive number that provides information about whether the reaction is in forward or backward direction.

$\gamma < 1$  : The reaction proceeds in the forward direction.

$\gamma = 1$  : The reaction is in equilibrium.

$\gamma > 1$  : The reaction proceeds in the backward direction.

Hence, the approach to equilibrium is defined as

$$\gamma K_2 = \frac{k_2}{k_{-2}} \quad (1.24)$$

Finally, using Eq. (1.17) with Eq. (1.24), the reaction rate is

$$R_2 = R = k_2 N K_1 p_A \theta_* - k_{-2} N \theta_* \frac{p_B}{K_3} = k_2 N \theta_* \left( K_1 p_A - \frac{p_B}{\gamma K_2 K_3} \right). \quad (1.25)$$

Two observations are made based on this derivation: First, it is almost impossible to determine the role of a catalyst by simply looking at the reaction equation. Second, an equation for a vastly simplified three-step-reaction already causes a fairly complex equation for R. Nevertheless, this model provides the possibility to define a single equation describing the reaction rate. The derivation becomes more complicated the more elementary steps a chemical reaction exhibits, but the result, a description of all processes condensed into a single equation, is all the more impressive. In the next section, this model will be applied to the reaction in question, methane pyrolysis.

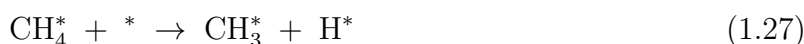
## 1.3 Methane pyrolysis

Methane pyrolysis and its individual reaction steps have been widely studied in the past [27, 28]. A catalytic decomposition process follows seven different elementary reaction steps, shown below, with the last step occurring twice per molecule. The sign “\*” always denotes a catalyst surface site, e.g.,  $\text{CH}_4^*$  is a methane molecule adsorbed on a catalyst.

Methane chemisorbs on the catalyst surface.



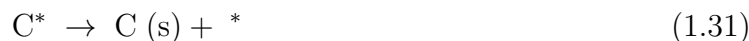
Chemisorbed methane dissociates into a methyl radical ( $\text{CH}_3$ ) and a hydrogen atom.



The methyl radical dissociates further into a methylene ( $\text{CH}_2$ ), and then into a methine ( $\text{CH}$ ) radical, followed by the last dissociation step to form adsorbed elemental carbon and hydrogen.



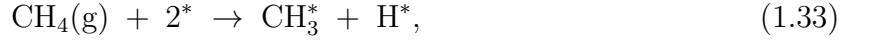
While carbon desorbs to form solid carbon, the hydrogen atoms recombine to produce hydrogen gas.



It is generally accepted that this is the pyrolysis reaction path, however it is still debated which reaction step is the slowest, and therefore rate-determining for the overall reaction. In the 1960s, Kozlov et al., doing single-pulse shock tube experiments, concluded that Eq. (1.28) is the rate-limiting step [29]. In contrast, some authors suggested that the rate-limiting

steps are carbon diffusion [30], and later surface transport [31]. Recent computational studies using Density Functional Theory calculations found Eq. (1.30) to be rate-determining [32], which will be used in this thesis.

Furthermore, two simplifications can be applied. Firstly, as shown by Fan et al. [32], Eq. (1.26) and Eq. (1.27) can be combined since the energy barrier for initial adsorption of methane is negligibly small. Hence the first reaction step is



reducing the number of steps to six. Secondly, the role of carbon desorption will be neglected. Carbon deposition on a catalyst surface is a complex phenomenon including adsorption, diffusion, segregation and precipitation, which in turn can cause formation of complex structures such as carbon nanotubes among many others [33, 34]. Thus, for practical reasons, the role of carbon in this context is greatly simplified by omitting (1.31) since it cannot be readily specified with the model presented. Moreover, the activity of carbon  $a_C$  is set to 1.

This leads to a system of five reaction steps whereby the fourth step, Eq. (1.30), is rate-determining. Four equilibrium constants can be derived as

$$K_1 = \frac{\theta_{\text{CH}_3}\theta_{\text{H}}}{p_{\text{CH}_4}\theta_*^2}, \quad (1.34)$$

$$K_2 = \frac{\theta_{\text{CH}_2}\theta_{\text{H}}}{\theta_{\text{CH}_3}\theta_*}, \quad (1.35)$$

$$K_3 = \frac{\theta_{\text{CH}}\theta_{\text{H}}}{\theta_{\text{CH}_2}\theta_*}, \quad (1.36)$$

$$K_5 = \frac{p_{\text{H}_2}\theta_*^2}{\theta_{\text{H}}^2} \quad (1.37)$$

where  $K_i$  is the equilibrium constant of reaction  $i$ ,  $\theta_j$  is the surface coverage of species  $j$ ,  $p_{\text{CH}_4}$  and  $p_{\text{H}_2}$  are partial pressures of  $\text{CH}_4$  and  $\text{H}_2$ , respectively. Keep in mind that partial pressures are always normalised with respect to the total system pressure. Subscript ‘\*’ always denotes a free surface site. From Eqs. (1.10) and (1.11)  $K_i$  is obtained as

$$K_i = \exp\left(-\frac{\Delta G_i^\circ}{k_{\text{B}}T}\right) = \exp\left(-\frac{\Delta E_i^\circ}{k_{\text{B}}T} + \frac{\Delta S_i^\circ}{k_{\text{B}}}\right) \quad (1.38)$$

For all intermediate steps where no gas-phase molecules are adsorbed or desorbed, namely (1.35) and (1.36), the entropy contributions are ignored because the entropy changes are negligibly small, i.e.,

$$\Delta G_i \approx \Delta E_i. \quad (1.39)$$

Reaction steps (1.34) and (1.37) require a different approach. To a good approximation, adsorbed molecules can be expected to lose all their entropy upon adsorption [14]:

$$\Delta S_{\text{ads}}^{\circ} = S_{\text{ads}}^{\circ} - S_{\text{gas}}^{\circ} \approx -S_{\text{gas}}^{\circ}. \quad (1.40)$$

Consequently, the same must apply in reverse for desorption. This will be important when compiling the final model in the results.

For Eqs. (1.34) to (1.37) there are now five unknown variables, i.e. all coverages  $\theta_j$ , but only four equations. A fifth equation can be obtained from the site-conservation rule which was defined in Eq. (1.20). Solving the system above yields four coverages which are all functions of  $\theta_*$ .

$$\text{From Eq. (1.37) : } \theta_{\text{H}} = \sqrt{\frac{K_5}{P_{\text{H}_2}}} \theta_* \quad (1.41)$$

$$\text{Eq. (1.34) with Eq. (1.41) : } \theta_{\text{CH}_3} = K_1 P_{\text{CH}_4} \sqrt{\frac{K_5}{P_{\text{H}_2}}} \theta_* \quad (1.42)$$

$$\text{Eq. (1.35) with Eq. (1.42) : } \theta_{\text{CH}_3} = K_1 K_2 K_5 \frac{P_{\text{CH}_4}}{P_{\text{H}_2}} \theta_* \quad (1.43)$$

$$\text{and Eq. (1.36) with Eq. (1.43) : } \theta_{\text{CH}} = K_1 K_2 K_3 K_5^{\frac{3}{2}} \frac{P_{\text{CH}_4}}{P_{\text{H}_2}^{\frac{3}{2}}} \theta_*. \quad (1.44)$$

Using Eq. (1.20) as a fifth equation with its general form of

$$\theta_* + \sum_{j \neq *} \theta_j = 1, \quad (1.45)$$

a fraction of  $j$ -covered sites can be defined as  $\lambda_j = \theta_j/\theta_*$  which leads to

$$\theta_* \left( 1 + \sum_{j \neq *} \lambda_j \right) = 1 \quad (1.46)$$

and the coverage of free sites can be expressed as

$$\theta_* = \left( 1 + \sum_{j \neq *} \lambda_j \right)^{-1}. \quad (1.47)$$

Inserting all terms from above yields

$$\theta_* = \left( 1 + K_1 P_{\text{CH}_4} \sqrt{\frac{K_5}{P_{\text{H}_2}}} + K_1 K_2 K_5 \frac{P_{\text{CH}_4}}{P_{\text{H}_2}} + K_1 K_2 K_3 K_5^{\frac{3}{2}} \frac{P_{\text{CH}_4}}{P_{\text{H}_2}^{\frac{3}{2}}} + \sqrt{\frac{K_5}{P_{\text{H}_2}}} \right)^{-1}. \quad (1.48)$$

The next step is to treat the only non-equilibrated reaction step (1.30). As shown in chapter 1.2.8, a reaction rate expression can be set up as

$$R_4 = k_4 \theta_{\text{CH}} \theta_* - k_{-4} \theta_{\text{H}} a_{\text{C}} \quad (1.49)$$

with  $a_C = 1$  and an approach to equilibrium  $\gamma_4$  as

$$\gamma_4 K_4 = \gamma_4 \frac{k_4}{k_{-4}} \quad (1.50)$$

leading to a reaction rate of

$$R_4 = k_4 \theta_{CH} \theta_* (1 - \gamma_4) \quad (1.51)$$

with  $k_4$  as

$$k_4 = \frac{k_B T}{h} \exp \left( -\frac{\Delta E_4^A}{k_B T} + \frac{\Delta S_4^A}{k_B} \right). \quad (1.52)$$

Having only one rate-determining reaction step allows for the important simplification of

$$\gamma_4 \approx \gamma \rightarrow R_4 \approx R \quad (1.53)$$

where  $\gamma$  is the approach to equilibrium for the overall reaction rate, i.e.,

$$\gamma = \frac{p_{H_2}^2}{K_{eq} p_{CH_4}} \quad \text{with} \quad K_{eq} = \exp \left( \frac{\Delta G_{rxn}}{k_B T} \right), \quad (1.54)$$

where  $p_{CH_4}$  and  $p_{H_2}$  are normalized partial pressures of methane and hydrogen respectively,  $K_{eq}$  the equilibrium constant and  $\Delta G_{rxn}$  is the Gibbs free energy of the overall reaction. Using Eq. (1.51) with Eqs. (1.4) and (1.5) for  $k_4$  leads the reaction rate as

$$R(T, p, \Delta E_C) = \frac{k_B T}{h} \exp \left( \frac{\Delta S_4^A}{k_B} \right) \exp \left( -\frac{\Delta E_4^A}{k_B T} \right) \theta_{CH} \theta_* (1 - \gamma) \quad (1.55)$$

with  $\Delta S_4^A$  and  $\Delta E_4^A$  as the reaction entropy and energy of non-equilibrated reaction step 4. While  $\Delta E_4^A$  follows the transition-state scaling relation that was already derived in chapter 1.2.5,  $\Delta S_4^A$  is more difficult to determine. As with Eqs. (1.35) and (1.36), the entropy contributions are neglected for step 4, i.e.  $\Delta S_4^A = 0$  because reactants and products stay in an adsorbed state. This leads to the final reaction rate equation

$$\boxed{R(T, p, \Delta E_C) = \frac{k_B T}{h} \exp \left( -\frac{\Delta E_4^A}{k_B T} \right) \theta_{CH} \theta_* (1 - \gamma).} \quad (1.56)$$

Impressively, this model describes the reaction rate as a combination of microscopic quantities such as adsorption and activation energy and macroscopic properties such as temperature and pressure. From  $R$  the volcano-shaped curve is obtained, the maximum position of which corresponds to an adsorption energy, which in turn is characteristic of a particular ideal catalyst material. In the next chapter, methods to obtain every parameter that is incorporated into this equation are discussed.



---

## Methodology

The main data source for the reaction equation of catalytic methane pyrolysis derived in chapter 1.3 is density functional theory (DFT) calculations. Literature values are used for the total reaction enthalpy and entropies. These values were determined experimentally decades ago and are generally available. All other values are based on DFT calculations. Due to its importance for this thesis, DFT will be the focus of the next chapter.

### 2.1 Density Functional Theory

In solid state physics, *ab initio* (lat.: ‘from the beginning’) calculations represent a generally recognised option to derive structural and dynamical properties of materials. For such calculations, exclusively fundamental laws of physics are being utilised. No parameters are optimised by empirical data fitting. The most famous example is the time-independent Schrödinger equation

$$\hat{H}|\psi\rangle = E|\psi\rangle, \quad (2.1)$$

given here in the Dirac notation, where  $|\psi\rangle$  is the wave function of a many-body system, i.e., a function that describes the quantum state of the system.  $\hat{H}$  is the Hamiltonian, an energy operator expressing kinetic and potential energy, and  $E$  the total energy of the system. In this form, the Schrödinger equation is written as an eigenvalue equation. If a wave function satisfies the equation, it is called a stationary state, or eigenstate of the system with a corresponding energy eigenvalue  $E$ . An eigenvalue corresponds to the value of an observable in this eigenstate, such as the system’s total energy. From the total energy, physical properties can be determined. Schrödinger equation is therefore the foundation for explaining properties of atoms, molecules, and solids [35].

While the Schrödinger equation yields excellent results for small molecules and small numbers of electrons, a system increase leads to the emergence of a so-called ‘exponential wall’, as Walter Kohn, a founding father of DFT, termed this phenomenon in his Nobel lectures [36].

Kohn pointed out that a system of 100 atoms would result in a minimization attempt for roughly  $10^{150}$  parameters. Since required computational power is not conceivable in the near future, finding an efficient strategy for calculating material properties is a high-priority goal in materials science.

An alternative approach that provides remedy to this exponential wall is density functional theory (DFT). While the Schrödinger equation is focused on the wave function of a system, DFT uses a semi-classical model where the wave function is replaced by an electron density function  $\rho(\mathbf{r})$ , from which the total energy  $E$  is computed.  $E$  is therefore a functional, i.e. a function that takes another function as an argument.

### 2.1.1 Hohenberg-Kohn theorems

Walter Kohn and Pierre Hohenberg were the pioneers of DFT. In their 1964 work, they derived two fundamental theorems that break down the many-electron problem to a mere function of electron density [37].

#### i) Existence theorem

Let  $\rho(\mathbf{r})$  be the ground-state single-particle electron density of an interacting electron system in an external potential  $V_{\text{ext}}(\mathbf{r})$ . Hohenberg and Kohn have shown that knowledge of  $\rho(\mathbf{r})$  implicitly determines  $V_{\text{ext}}(\mathbf{r})$ , which in turn determines the Hamiltonian  $\hat{H}$ .  $\hat{H}$  allows for calculation of all ground-state properties of the system. Therefore,  $V_{\text{ext}}(\mathbf{r})$  is a unique functional of the ground-state density  $\rho(\mathbf{r})$ . In other words, the energy functional  $E[\rho(\mathbf{r})]$  of a system can be derived from one function only, namely the particle density  $\rho(\mathbf{r})$  [35].

#### ii) Variational principle

The energy functional  $E[\rho(\mathbf{r})]$  in a system of a given density  $\rho(\mathbf{r})$  that integrates to the correct number of electrons satisfies the relation  $E[\rho(\mathbf{r})] \geq E_0$ , where  $E_0$  is the true ground-state energy of the system. Hence, the total energy of a  $N$ -electron system can be minimised by varying the ground-state electron density  $\rho(\mathbf{r})$ . By minimizing the density function using variational principle, which is a function of three variables instead of the many-body wavefunction with  $3N$  variables [35], the given problem is drastically simplified.

### 2.1.2 Kohn-Sham equations

Both findings led to the derivation of the so-called Kohn-Sham equation, named after Walter Kohn and Lu Jeu Sham [38]:

$$\hat{H}_{\text{KS}}\psi_i = \epsilon_i\psi_i. \quad (2.2)$$



Looking very similar to Schrödinger equation, it describes a fictitious system of non-interacting particles with  $\hat{H}_{\text{KS}}$  as the Kohn-Sham Hamiltonian,  $\epsilon_i$  energy eigenvalues of the system and  $\psi_i$  Kohn-Sham orbitals for which it is true that

$$\rho(\mathbf{r}) = \sum_{i=1}^N \psi_i^*(\mathbf{r})\psi_i(\mathbf{r}), \quad (2.3)$$

where  $N$  is the number of electrons in the system. Eq. 2.2, upon minimization, corresponds to the true ground-state energy of a system according to the variational principle. Thus, the Kohn-Sham equation is the Schrödinger equation of a system of non-interacting particles that generate the same density as a given system of interacting particles.

A critical part in these minimization calculations is the definition of an accurate Kohn-Sham Hamiltonian

$$\hat{H}_{\text{KS}} = E_{\text{kin}} + V_{\text{e-nuc}}(\mathbf{r}) + V_{\text{H}}(\mathbf{r}) + V_{\text{XC}}(\mathbf{r}). \quad (2.4)$$

$E_{\text{kin}}$  represents the kinetic energy,  $V_{\text{e-nuc}}(\mathbf{r})$  the Coulomb potential caused by the electron-nuclei interaction,  $V_{\text{H}}(\mathbf{r})$  is the Hartree potential and  $V_{\text{XC}}(\mathbf{r})$  is the exchange-correlation potential [39]. The last term,  $V_{\text{XC}}(\mathbf{r})$ , incorporates all quantum-mechanical effects. This includes phenomena caused by the fermionic nature of electrons, i.e. exchange effects, such as the Pauli exclusion principle. Discrepancies between systems of interacting and non-interacting particles, also known as correlation effects, are also part of  $V_{\text{XC}}(\mathbf{r})$ . Advancements in the derivation of an accurate exchange-correlation potential have led to desired results of chemical accuracy, i.e. the accuracy required to make reasonable chemical predictions, which is around 4 kJ/mol or 0.04 eV/at. [35]. The two main types of exchange correlation functionals are the Local Density Approximation (LDA) and the General Gradient Approximation (GGA), with the latter being used for all calculations in this thesis. For further details, the reader is referred to secondary literature [40].

Kohn-Sham equations are characterised by a straightforward algorithm design. An initial guess for the electron density is made, which is used for the calculation of the corresponding potential. With this potential the Kohn-Sham equation is being solved, yielding energy eigenvalues  $\epsilon_i$  and Kohn-Sham orbitals  $\psi_i$ . From this result, a new electron density can be computed from this result. The algorithm is repeated until a predefined tolerance in total energy change is reached.

## 2.2 VASP

The Vienna Ab initio Simulation Package (VASP) was used for all DFT calculations in this work [41]. In VASP, four specific input files must be provided to perform a DFT calculation: INCAR, KPOINTS, POSCAR and POTCAR. It is important to provide enough information to enable seamless repeatability, hence each file will hereafter be discussed in detail:

### 2.2.1 INCAR

The INCAR file is the central input file of VASP. It determines the type of calculation and how it is performed. In INCAR files, tags are used to determine algorithms and parameters. Over 400 different tags can be used in VASP, which permits a high degree of customization. Most parameters were retained in their default settings. The most important tags as well as the ones that were changed for conducted calculations are described below.

- **ALGO = Fast:** **ALGO** sets the electronic minimization algorithm. More than twenty different algorithms are available. 'fast' is a mixture of the Davidson [42] and RMM-DIIS algorithms [43], where Davidson is initially used and then replaced by RMM-DIIS.
- **EDIFF =  $10^{-4}$ :** **EDIFF** specifies the total energy change in eV per simulation box and the band structure energy change between two steps that triggers a break in the electronic self-consistency loop when it is undershot. For high-precision calculations, such as for PES, this value was decreased to  $10^{-6}$ .
- **EDIFFG =  $10^{-4}$ :** **EDIFFG** determines the break condition for the ionic relaxation loop. The default value is ten times **EDIFF**.
- **GGA = RP:** The **GGA** tag determines the exchange-correlation functional that is used for calculation. Either a General Gradient Approximation (GGA) or Local Density Approximation (LDA) functional can be used. For this thesis, all calculations were carried out using GGA exchange-correlation functional, parametrised by Perdew Burke Ernzerhof (PBE-GGA) [44], that was revised by Hammer et al. to improve chemisorption energetics of atoms and molecules on transition-metal surfaces [45]. A projector augmented wave (PAW) method was used for electron-ion interactions [46].
- **IBRION = 2:** **IBRION** how the structure is optimized. A value of 2 means that a conjugate-gradient algorithm is used to approach ground-state energy.
- **ICHARG = 2:** The tag **ICHARG** determines the initial charge density. **ICHARG = 2** is the default setting in VASP and creates superposition of atomic charge densities.

- **IMAGES = 8**: In order to calculate activation energies for reaction steps, the nudged elastic band (NEB) method is used which will be explained in chapter 2.3.4. The number of images defines the resolution of the reaction path.
- **ISIF = 2**: ISIF specifies if the stress tensor is calculated and which degrees of freedom are allowed. In VASP, positions, cell shape and cell volume can be enabled to change during relaxation. ISIF = 2 fixes the cell shape and volume while allowing atoms to change their positions.
- **ISTART = 0**: ISTART determines whether precalculated orbitals are used, which are provided via the WAVECAR file, or whether the orbitals are initialised at the beginning, which is indicated by the number 0.
- **LREAL = Auto**: LREAL specifies whether calculations are carried out in real or reciprocal space. While in reciprocal space the number of operations scales with the number of plane waves, in real space the projection operators are confined to spheres around each atom. Thus the number of operations does not increase with system size in real space, however this requires optimised projection operators. LREAL = Auto ensures fully automatic optimization of projection operators.
- **LWAVE = False**: This determines whether the wavefunctions are written to the WAVECAR file at the end of a run. False skips this step.
- **MAGMOM = 36\*2.84 2\*0.0**: MAGMOM is only used for elements that are ferro- or paramagnetic and is used together with ISPIN = 2. An initial magnetic moment is assigned to each atom. For instance, the given tag was used for a fcc-Fe structure with 36 atoms and a CH molecule as an adsorbate. fcc-Fe is paramagnetic with an initial magnetic moment of 2.84 Bohr magneton  $\mu_B$  [47]. All numbers were taken from the website Materials Project ([www.materialsproject.org](http://www.materialsproject.org)), an open dataset for properties of inorganic materials [48].
- **NCORE = 2**: NCORE allows for better parallelization by setting the number of cores that work on an individual orbital.
- **NELM = 100**: NELM sets the maximum number of electronic self-consistency steps. The default value is 60 and normally convergence should be achieved within about 50 steps. Due to convergence problems in the initial calculations, NELM was increased to 100 and not changed back afterwards.
- **NSW = 20**: NSW determines the maximum number of ionic steps during relaxation.
- **SPRING = -5**: SPRING is used for nudged elastic band calculations and defines the geometrical constraints of each individual image.

### 2.2.2 KPOINTS

The KPOINTS file determines the number of Bloch vectors, also known as k-points that are used to sample the Brillouin zone. A  $\Gamma$ -centered k-mesh of 6x6x1 was chosen with  $k(z)=1$  due to lack of symmetry in z-direction.

### 2.2.3 POSCAR

The POSCAR file serves as an input file determining the lattice geometry and atomic positions. The first line provides information about the elements that are in the cell as well as their quantity, hence a total of 38 atoms are in this input file.

```
Fe36 H1 C1
```

While 1.0 is the lattice scaling factor, the next three lines represent the scaled lattice vectors of the cell.

```
1.0
6.698130 0.000000 3.867167
2.232710 6.315057 3.867167
0.000000 0.000000 35.312445
```

The first two lines again indicate present elements, but also indicate the order of their respective positions that will follow below. **Selective dynamics** indicates that only some elements will be allowed to move during relaxation calculations while **Direct** means the positions are provided in fractional coordinates.

```
Fe H C
36 1 1
Selective dynamics
direct
```

Two of the 38 atoms are taken out as examples. While the Fe atom is fixed to its position, as indicated by **F F F** (**F** = “False”), the H atom is movable in all three spatial directions (**T** = “True”).

```
0.000000 0.000000 0.000000 F F F Fe
0.057377 0.057377 0.294604 T T T H
```

### 2.2.4 POTCAR

The POTCAR file contains the pseudopotential for each atomic species used in the calculation. The POTCAR files are concatenated if more than one species is present. The file also contains information about the atoms, including their mass, the number of their valence electrons, or the energy of the reference configuration for which the pseudopotential was created. The pseudopotentials are distributed as a part of VASP.

## 2.3 Approach

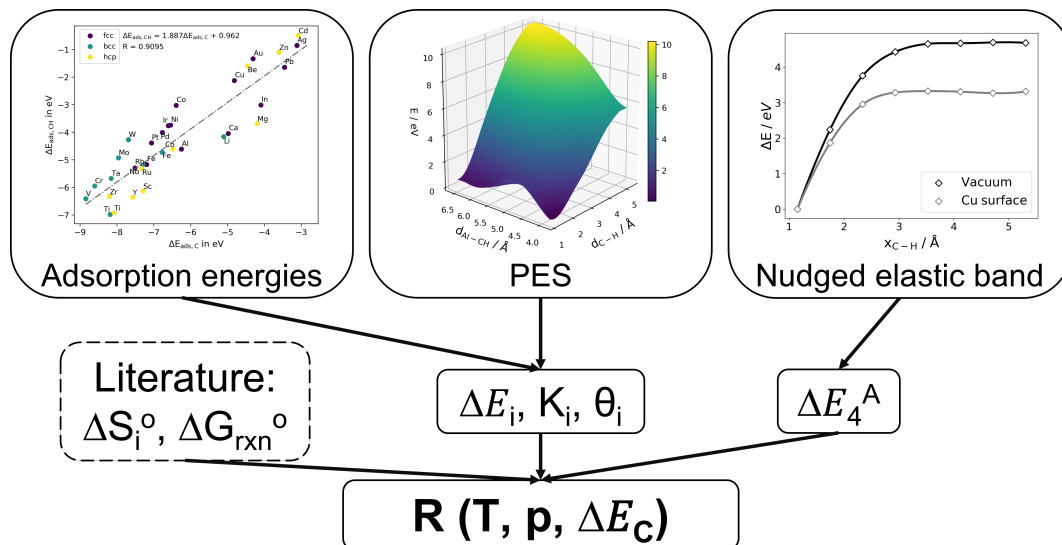


Figure 2.1: Flowchart illustrating the process for determining the reaction rate in catalytic methane pyrolysis.

DFT is used to calculate most of the values required to obtain a complete equation for the reaction rate  $R$ . As an overview, a flowchart is shown in Fig. 2.1. Surface adsorption energies for all relevant adsorbates (C, H, CH, CH<sub>2</sub>, CH<sub>3</sub> and CH<sub>4</sub>) on many different substrates are calculated to obtain adsorption energy trends. By the use of PES calculations, reaction energies are determined for each elementary step. Both are the foundation to calculate surface-dependent equilibrium constants  $K_i$  and coverages  $\theta_i$ . Activation energy for reaction step 4,  $\Delta E_4^A$ , is obtained from nudged elastic band calculations. Along with standard reaction enthalpies and entropies for each reaction step taken from literature,  $R$  can be computed.

### 2.3.1 Molecular energies

First, all the total energies of the molecules,  $E_{\text{mol}}$ , that are present during any elementary step in methane pyrolysis reaction are calculated. The molecules examined are C, H, CH, CH<sub>2</sub>, CH<sub>3</sub>, CH<sub>4</sub> and H<sub>2</sub>. Each molecule is put inside of a cubic simulation cell with an edge length of 10 Å and relaxed. The energies also provide a basis for the calculation of chemical reaction energies according to Eq. (1.8).

### 2.3.2 Adsorption energies

The adsorption energy can be calculated as

$$E_{\text{Ads}} = E_{\text{mol+slab}} - E_{\text{mol}} - E_{\text{slab}} \quad (2.5)$$

## 2.3 Approach

where  $E_{\text{Ads}}$  is the adsorption energy of a specific molecule-substrate pair.  $E_{\text{slab}}$  and  $E_{\text{mol+slab}}$  are the total energies of simulation cells containing only the substrate, and both adsorbant and substrate combined with a well-defined distance apart, respectively [49].

Final structures of combined slab and molecule must be checked for possible relaxation errors. If the distance between molecule and surface is too small and the substrate attracts the molecule very strongly, the molecule may even be absorbed. This is particularly relevant for individual C and H atoms. On the other hand, if the distance is too large, there could be no interaction at all. In both cases, calculated adsorption energies are invalid. This is the reason why distances for different adsorbates and substrates vary.

Input files are generated using the open-source Python library Pymatgen and computed at the Vienna Scientific Cluster (VSC), a high-performance computing cluster system. Three different crystal structures are considered: face-centered cubic, body-centered cubic and hexagonal close-packed. In total, 30 different elements are examined. For each element, supercells with a size of  $2 \times 2 \times 4$  for a (001)-surface and  $3 \times 3 \times 4$  for a (111)-surface are generated, causing the supercells to contain between 36 and 96 substrate atoms depending on the crystal structure and orientation, with  $25 \text{ \AA}$  of vacuum above the surface to prevent any effects due to periodic boundary condition along the c-axis. From these structural relaxations, total energies of the substrate slabs with vacuum,  $E_{\text{slab}}$ , are obtained.

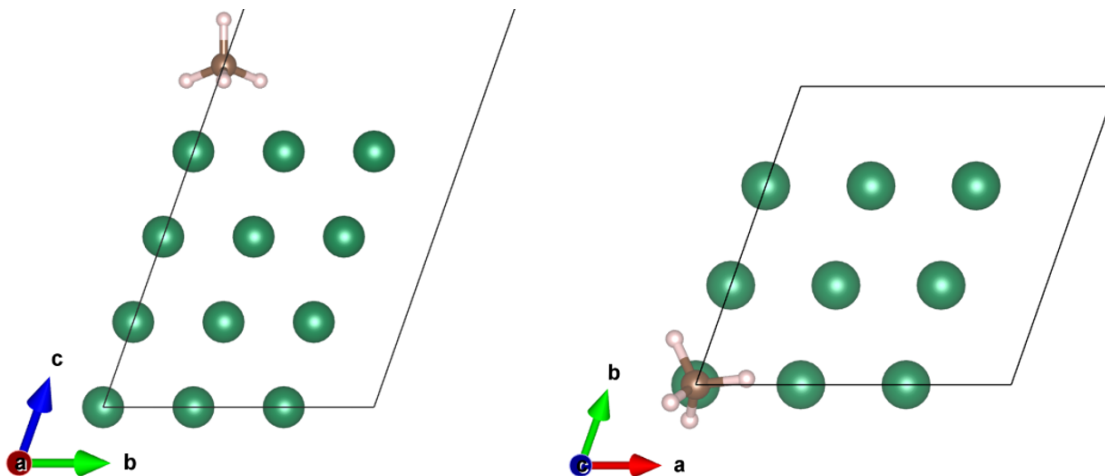


Figure 2.2: Simulation cell including a  $\text{CH}_4$  molecule on top of a (111)-Ni surface composed of  $3 \times 3 \times 4$  unit cells, viewed along the a-axis (left) and c-axis (right).

The relaxed molecules described in section 2.3.1 are then placed above a previously relaxed surface slab. The atom of the molecule closest to the surface is between  $2$  and  $3.5 \text{ \AA}$  away from the closest surface atom. The molecules are orientated so that a maximum amount of hydrogen atoms is located as close to the surface as possible. An exemplary simulation cell is shown in Fig. 2.2. The combined structure of slab and molecule is relaxed again and the total energy  $E_{\text{slab+mol}}$  is obtained. The first two atomic layers and the molecule

are allowed to move in all three spatial directions, while the rest of the substrate is fixed. Such a calculation is carried out for both surface orientations (001) and (111) and every adsorbate-substrate-pair.

### 2.3.3 PES calculations

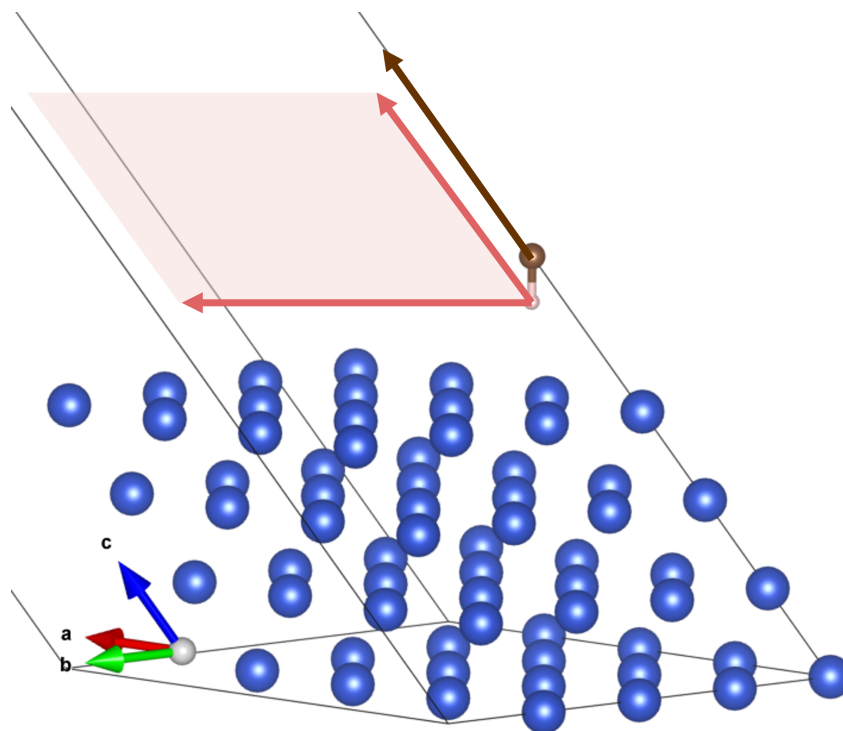


Figure 2.3: Illustration of the scanned area during PES calculation for CH: While the C atom only moves along the brown arrow in the c-direction, the H atom is also moved in between a- and b-axes indicated by the pink area.

Potential energy surfaces are calculated in a similar way. A (111)-surface of fcc-Cu is used for all calculations with a supercell size of  $3 \times 3 \times 4$ , yielding 64 Cu atoms. A molecule is again placed on the surface and the structure is subjected to a relaxation calculation. After relaxation, 10 structures are created, all differing in the distance of the relaxed molecule from the surface. The distance is increased in a regular way along the c-axis by  $0.3 \text{ \AA}$  per structure, so that the tenth structure is  $3 \text{ \AA}$  further from the initial relaxed position. While the KPOINTS file remained unchanged, EDIFF in the INCAR file was decreased to  $10^{-6}$  to improve accuracy.

For each of these ten structures, ten additional structures are created in which an H atom is successively removed from the molecule of interest. For each molecule, it is ensured that the atom is removed as far as possible due to the periodic boundary conditions which is approximately at the center of the unit cell. This results in 100 structures and calculations per PES. This scanning procedure is performed for CH, CH<sub>2</sub> and CH<sub>3</sub>. In the structures, the

central C atom is fixed while the receding H atom is still allowed to move in the z direction to detect adsorption phenomena. All other H atoms in CH<sub>2</sub> and CH<sub>3</sub> are allowed to move freely so that molecular relaxations can occur. A schematic illustration is shown in Fig. 2.3 where the H atom scanned area is shown by a semi-transparent pink parallelogram. The C atom only moves along the brown arrow which is perpendicular to the c-axis. From the PES calculations, the parameter  $\xi$  in the adsorption energy scaling relations for Eqs. 1.7 and 1.8 can be obtained.

### 2.3.4 Nudged elastic band calculations

In order to obtain the activation energy for CH dissociation  $\Delta E_4^A$  that is a component of the reaction rate equation (1.56), nudged elastic band calculations (NEB) are carried out. NEB is a method to find the transition state of a chemical reaction by generating an energy profile along a reaction path [50]. We used its implementation directly in the VASP package. A POSCAR file is generated for known initial and final states. In between, equidistant images along the reaction path images are created. The method optimises the energy of each intermediate image along the reaction path by adding spring forces between images and maintaining equal distances to neighbouring images.

Two NEB calculations are performed. The first run uses ten POSCAR files that were closest to the surface in the PES calculation for CH and fcc-Cu. The second run uses the same POSCAR files again, but every Cu atom was removed from the POSCAR files. In order to run a NEB calculation, the INCAR parameter `IMAGES` for the number of images between initial and final structure was set to 8. `SPRING`, which defines the ‘spring constant’, was kept at its default value of  $-5$ .



# Results

## 3.1 Model input calculations

### 3.1.1 Molecular energies

The total energy for each individual and isolated species was calculated according methodological approach described in chapter 2.3.1. The resulting energies per molecule are presented in the table below.

	C	CH	CH <sub>2</sub>	CH <sub>3</sub>	CH <sub>4</sub>	H	H <sub>2</sub>
E / eV	-1.291	-6.086	-12.09	-18.18	-24.01	-1.105	-6.689

Table 3.1: Total energies of all species in eV that are in involved in the methane pyrolysis reaction.

These energies can now be used to calculate the reaction energies of each individual elementary step. In the following table, the computed reaction energies are listed together with the tabulated values from literature. The values  $\Delta E_{\text{ref},0}$  are results from DFT calculation, while  $\Delta E_{\text{ref},1}$  are experimental values.

	$\Delta E_{\text{calc}}$ eV	$\Delta E_{\text{ref},0}$ [51] eV	$\Delta E_{\text{ref},1}$ [52] eV	$\epsilon_{\text{calc-ref},1}$ eV	$\eta_{\text{calc-ref},1}$
$\text{CH}_4(\text{g}) \rightarrow \text{CH}_3(\text{g}) + \text{H}(\text{g})$	4.725	4.906	4.56	0.165	3.5%
$\text{CH}_3(\text{g}) \rightarrow \text{CH}_2(\text{g}) + \text{H}(\text{g})$	4.985	5.128	4.788	0.197	3.9%
$\text{CH}_2(\text{g}) \rightarrow \text{CH}(\text{g}) + \text{H}(\text{g})$	4.899	4.654	4.394	0.505	10.3%
$\text{CH}(\text{g}) \rightarrow \text{C}(\text{g}) + \text{H}(\text{g})$	3.690	3.621	3.5133	0.177	4.7%
$2\text{H}(\text{g}) \rightarrow \text{H}_2(\text{g})$	-4.479	-	-4.527	-0.048	-1.1%

Table 3.2: Comparison of calculated reaction energies with experimental energies from the literature.

Overall, the calculated energies agree well with the experimentally determined reaction energy values and the data from the DFT reference study. The agreement of the calculated values with the experimental values is more accurate for the first two reaction steps than in the DFT reference study, while it is worse for the following two steps. The most striking

difference is the change in reaction energy for  $\text{CH}_2$  dissociation. While all other relative discrepancies are below 5%, the deviation in this reaction step is slightly over 10%. However, since the purpose of this work is to express the reaction rate as a function of computational values, the deviating values will further be used consecutively.

### 3.1.2 Adsorption energy trends

Calculated adsorption energies as described in chapter 2.3.2 are presented below. Fig. 3.1 depicts adsorption energies for a given molecule as a function of carbon adsorption energy for a given substrate element. Each point is labeled with the corresponding element. In the lower right corners of each graph, the Pearson correlation coefficient and the linear function are shown which will be used for the Sabatier model at a later point. The three crystal structures considered, face-centered cubic (fcc), body-centered cubic (bcc) and hexagonal close-packed (hcp) systems all have a close-packed surface structure, i.e., (111) for fcc and bcc and (0001) for hcp, respectively. A complete list of all energy values can be found in table 3.3.

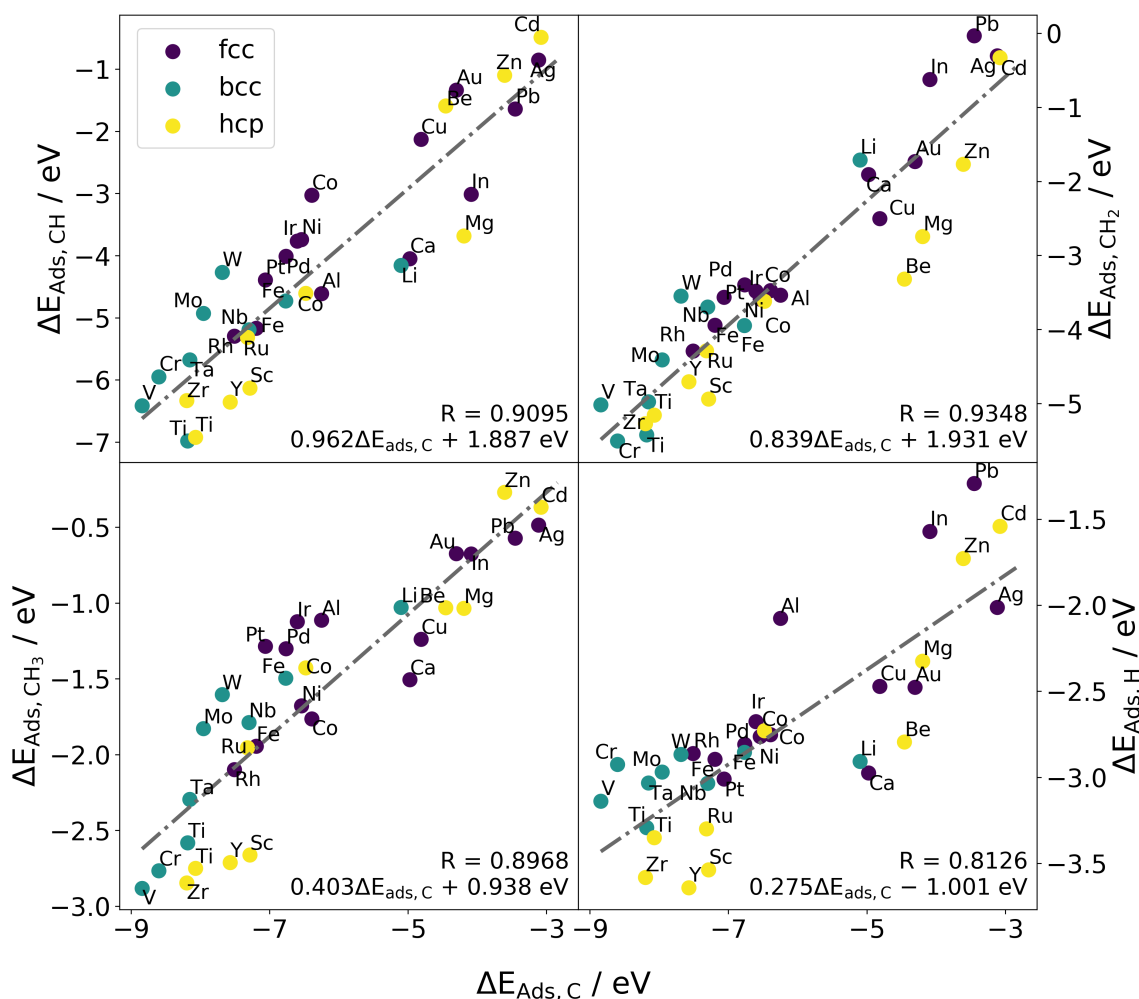


Figure 3.1: Adsorption energies of  $\text{CH}$ ,  $\text{CH}_2$ ,  $\text{CH}_3$  and  $\text{H}$  as a function of  $\Delta E_{\text{Ads,C}}$  for face-centered cubic (fcc), body-centered cubic (bcc) and hexagonal close-packed (hcp) substrate structures and close-packed surface planes.

Element	$\Delta E_{\text{Ads,C}}$ eV	$\Delta E_{\text{CH}}$ eV	$\Delta E_{\text{CH}_2}$ eV	$\Delta E_{\text{CH}_3}$ eV	$\Delta E_{\text{H}}$ eV
V	-8.842	-6.413	-5.018	-2.881	-3.138
Cr	-8.601	-5.949	-5.504	-2.766	-2.925
Zr	-8.199	-6.330	-5.273	-2.845	-3.580
Ti (bcc)	-8.183	-6.923	-5.155	-2.749	-3.351
Ta	-8.153	-5.675	-4.977	-2.295	-3.031
Ti (hcp)	-8.072	-6.923	-5.155	-2.749	-3.351
Mo	-7.958	-4.927	-4.410	-1.828	-2.969
W	-7.685	-4.267	-3.547	-1.603	-2.866
Y	-7.572	-6.353	-4.706	-2.710	-3.642
Rh	-7.509	-5.294	-4.293	-2.099	-2.86
Ru	-7.319	-5.316	-4.286	-1.954	-3.298
Nb	-7.301	-5.194	-3.697	-1.788	-3.033
Sc	-7.286	-6.129	-4.938	-2.661	-3.537
Fe (fcc)	-7.195	-4.726	-3.946	-1.496	-2.853
Pt	-7.061	-4.389	-3.566	-1.286	-3.009
Fe (bcc)	-6.770	-4.726	-3.946	-1.496	-2.853
Pd	-6.765	-4.009	-3.397	-1.301	-2.808
Ir	-6.603	-3.764	-3.484	-1.124	-2.675
Ni	-6.541	-3.741	-3.591	-1.677	-2.762
Co (hcp)	-6.480	-4.606	-3.621	-1.427	-2.729
Co (fcc)	-6.393	-4.606	-3.621	-1.427	-2.729
Al	-6.249	-4.612	-3.536	-1.112	-2.076
Li	-5.101	-4.158	-1.709	-1.028	-2.907
Ca	-4.977	-4.048	-1.908	-1.506	-2.974
Cu	-4.813	-2.127	-2.503	-1.238	-2.471
Be	-4.457	-1.590	-3.319	-1.030	-2.795
Au	-4.305	-1.336	-1.729	-0.675	-2.477
Mg	-4.193	-3.681	-2.746	-1.034	-2.324
In	-4.091	-3.012	-0.625	-0.676	-1.571
Zn	-3.607	-1.097	-1.769	-0.269	-1.729
Pb	-3.452	-1.641	-0.033	-0.571	-1.292
Ag	-3.117	-0.853	-0.301	-0.487	-2.012
Cd	-3.079	-0.484	-0.329	-0.367	-1.540

Table 3.3: Adsorption energies in eV for all molecule-substrate combinations that have been computed. The list is presented in descending order of  $\Delta E_{\text{Ads,C}}$  magnitude.

The three hydrocarbon diagrams (both top and lower left in Fig. 3.1) show a reasonable correlation between molecule and carbon adsorption energies with values for the Pearson correlation coefficient  $R$  of approximately 0.9. This indicates a strong correlation validating the use of a linear scaling model for subsequent calculations.

Hardly any difference can be seen between different crystal structures, indicating an overall trend that depends on the adsorption energy of the carbon base atom and whether the surface is close-packed or not, rather than on the given crystal structure. However it is noticeable that bcc structures tend to be more clustered while fcc and hcp structures are stretching over a wider range of carbon adsorption energies.

An interesting finding is the apparent gap of around 1 eV between  $-6$  and  $-5$  eV which is not populated by any single element. In future studies, yet more elements and alloys might be included in the model to find out if this is an actual phenomenon or coincidence.

The adsorption energies for carbon and hydrogen (lower right graph in Fig. 3.1) show weaker correlation than the hydrocarbons. This is not surprising considering that C and H react very differently due to their different chemical properties, e.g., their respective van der Waals contributions [53]. Nevertheless, there is still a reasonable correlation with  $R > 0.8$ , indicating a dominance of substrate element properties over the adsorbed element that determines adsorption energy.

As a comparison to Fig. 3.1, Fig. 3.2 shows adsorption energy trends for fcc, bcc and cubic diamond (cd) substrate structures, but with a (001) surface plane. Since no crystallographic plane proves to be comparable, no hexagonal close-packed structures are calculated. Linear relations vary significantly between both systems. Slopes differ between approximately 0.4 and 1 while the y-intercepts show discrepancies between 0.05 and 0.3 eV.

When considering Pearson correlation coefficients, the overall correlation is weaker compared to dense packed areas. This becomes more obvious for the relation between C and H adsorption energies, where  $R$  drops to 0.58. The number of outliers is also clearly increasing for all four plots in Fig. 3.2. Without any doubt, close-packed structures show better correlation compared to (001) surfaces, rendering them the preferred choice for determining linear adsorption energy trends. Thus, scaling relations from Fig. 3.1 will be used for further investigations.

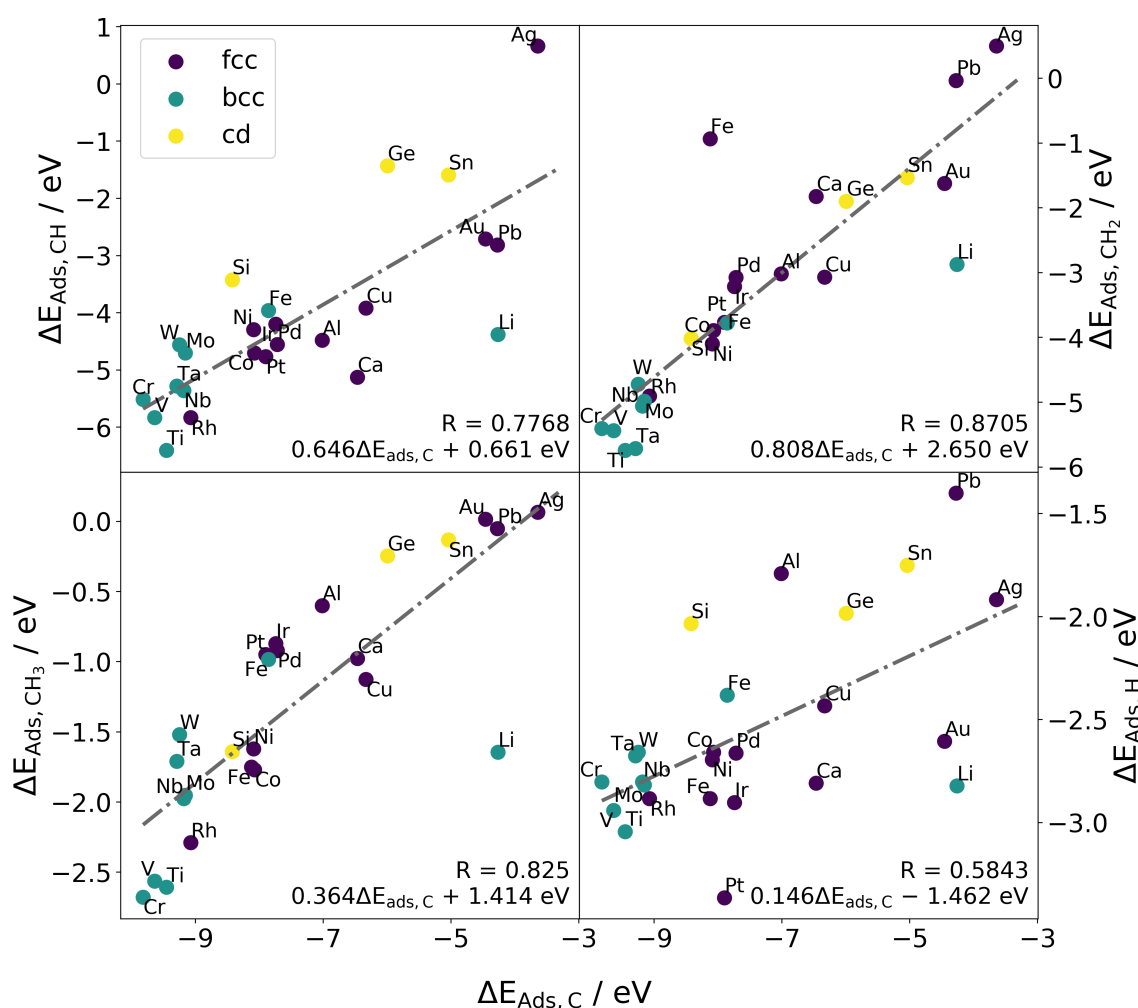


Figure 3.2: Adsorption energies of CH, CH<sub>2</sub>, CH<sub>3</sub> and H as a function of  $\Delta E_{\text{Ads,C}}$  for face-centered cubic (fcc), body-centered cubic (bcc) and cubic diamond (cd) substrate structures, all with (001) surface plane.

### 3.1.3 Chemical correlations

A striking trend in adsorption energies is visible when taking a closer look at the periodic table. Most of the elements calculated are transition metals located in the d-block, i.e., in groups 3 to 12. Fig. 3.3 illustrates this relationship by color-coding each element according to their position in the d-block. Elements that are not included in the d-block are greyed out. In general, it can be stated that the further left an element is positioned in the d-block, the more negative are its adsorption energies.

One explanation for this clearly visible trend can be derived from the chemistry of transition metals. Transition metals are mainly characterized by their partially filled d-subshells. Due to the directional character of d-orbitals, the nucleus is weakly shielded, interactions between d-electrons are weak and the nucleus does not only strongly attract d- but also s-electrons from the next higher s-orbital. This results in relatively high but slowly increasing ionization

energies over a given period [54], which in turn inhibits reactivity. This is evident when considering enthalpies of hydration, which decrease with a higher group number [55]. This drop in reactivity could also be a reason for the lower adsorption energies. No correlation is found between other element properties such as the Pauling electronegativity scale or atomic radius and adsorption values. Electronegativity values and atomic radii were taken from the National Library of Medicine [56].

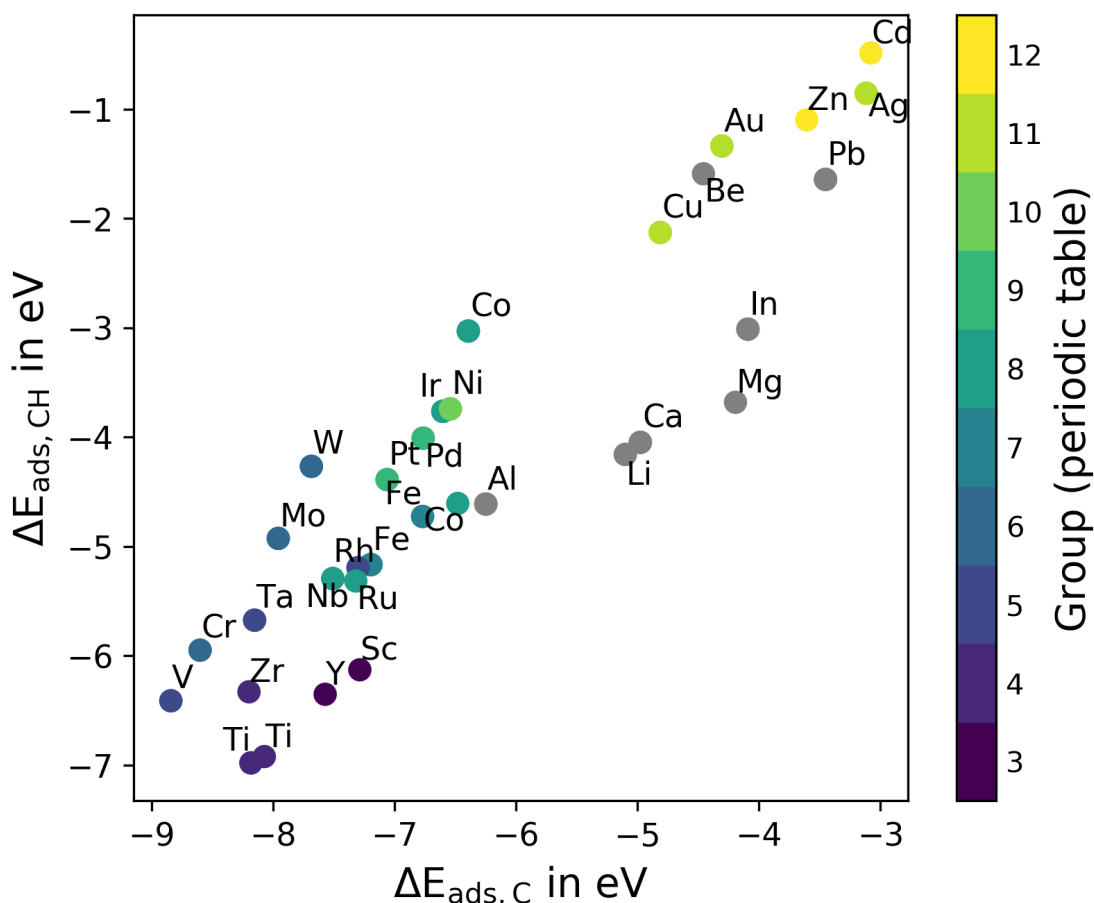


Figure 3.3:  $\Delta E_{\text{Ads,CH}}$  as a function of  $\Delta E_{\text{Ads,C}}$  for different substrates. For d-block elements, correlation between group number and their adsorption energy is clearly evident.

### 3.1.4 PES

As described in chapter 1.2.5, Eq. (1.7) and (1.8) are both a function of the carbon adsorption energy  $\Delta E_{\text{Ads,C}}$ , the slope in the adsorption energy scaling relation as seen in Fig. 3.1 and the parameter  $\xi$ .  $\xi$  can be obtained from potential energy surfaces, which were calculated according to the methodological approach described in chapter 2.3.3. The calculations were carried out for a (111)-surface of fcc-Cu. The resulting grids of 10 x 10 energy values was then interpolated with a cubic spline. Results are shown in Fig. 3.4. While the x-axis depicts the increasing distance between  $\text{CH}_x$  ( $x = 0, 1, 2$ ) and H during the dissociation reaction, the y-axis shows the distance between the surface and the C atom of the molecule.

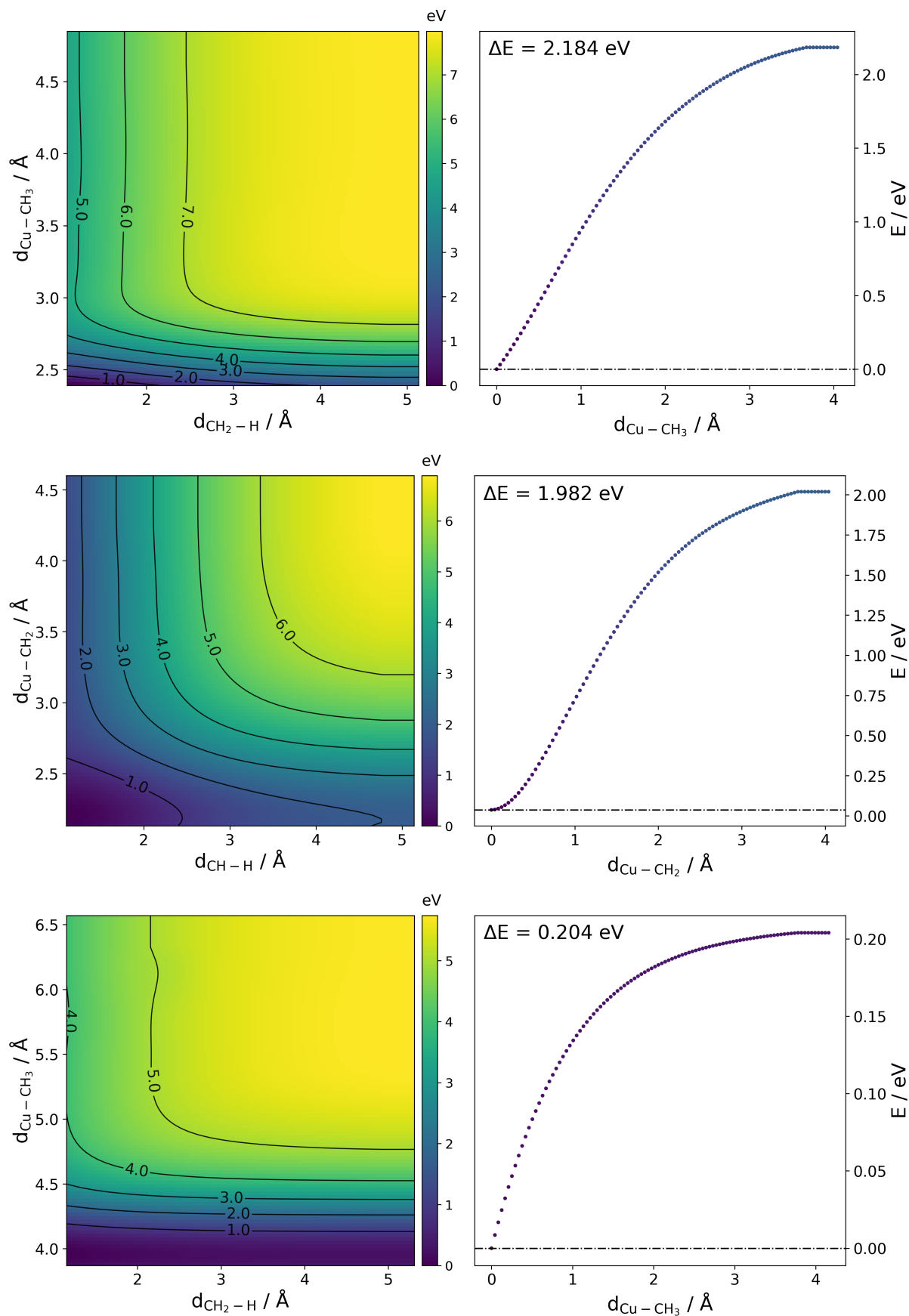


Figure 3.4: Left: PES for  $\text{CH}_3$ ,  $\text{CH}_2$  and  $\text{CH}$  dissociation over Cu (111). Right: Potential energy curves for respective dissociation reactions in their adsorbed state, i.e., their state of minimal calculated energy.

First of all, Cu shows a decrease in dissociation energy for all three considered elementary steps. The dissociation energy for the adsorbed state that is mapped in the right graphs in Fig. 3.4 is decreasing for each additional reaction step with a big leap between CH<sub>2</sub> and CH. The low dissociation energy is particularly surprising, since it contradicts the proposed model that CH dissociation is the rate-determining step. The change in dissociation energy as a function of distance is also striking. While the effect of the Cu surface on CH<sub>3</sub> starts at relatively small distances, the effect on CH is more gradual, with CH<sub>2</sub> being an extreme example showing a change in dissociation energy up to 1 Å further away from the equilibrium position.

### 3.1.5 Free site coverage $\theta_*$

The most important data for the model that is obtained from these calculations are the adsorbed dissociation energies that are displayed in the top left corner of the right plots in Fig. 3.4. Together with the scaling slopes from Fig. 3.1, adsorption-dependent reaction energies for the second (Eq. (1.28)) and third (Eq. (1.29)) elementary steps, i.e. the respective dissociations of the CH<sub>3</sub> and CH<sub>2</sub> radicals, can now be calculated with Eq. (1.8), which is

$$\Delta E = \sum_{i=1}^N (\Delta \gamma_i \Delta E^{A_i}) + \Delta \xi.$$

For Eq. (1.28),  $\Delta \gamma$  is obtained from the slopes of the adsorption energy scaling relations in Fig. 3.1,

$$\Delta \gamma_2 = \gamma_{\text{CH}_2} - \gamma_{\text{CH}_3} = 0.839 - 0.403 = 0.436.$$

For  $\Delta \xi_2$ , scaling relation, PES and the total energies of the isolated molecules are used. The carbon adsorption energy of Cu is taken from Table 3.3 with a corresponding  $\Delta E$  of 2.814 eV. This is the reaction energy for the adsorbed dissociation reaction of CH<sub>3</sub>. The value is shown in Fig. 3.4 in the upper right graph. Together with the calculated dissociation reaction that can be taken from Table 3.2, the linear function can be written as

$$\Delta E_2 = 0.436 \Delta E_{\text{Ads,C}} + 4.28 \text{ eV.} \quad (3.1)$$

For all intermediate steps where no gas phase molecules are adsorbed or desorbed, the entropy contributions are neglected, which results in  $\Delta G_2$  as

$$\Delta G_2 \approx \Delta E_2 = 0.436 \Delta E_{\text{Ads,C}} + 4.28 \text{ eV.} \quad (3.2)$$

The subscript 2 denotes the second reaction step of the catalytic pyrolysis reaction. Analogously, the same procedure is carried out for reaction step 3, yielding

$$\Delta G_3 \approx \Delta E_3 = 0.123 \Delta E_{\text{Ads,C}} + 2.57 \text{ eV.} \quad (3.3)$$



Reaction steps 1 and 5 require a different approach since reaction energies for both  $\text{CH}_4$  and  $\text{H}_2$  are not functions of  $\Delta E_{\text{Ads,C}}$ . Therefore, the values from Table 3.2 are directly used as reaction energies. Both are, however, functions of entropy since their reaction steps involve adsorption and desorption phenomena, respectively. As shown in chapter 1.3,  $\Delta S_{\text{ads}}^{\circ} \approx -S_{\text{gas}}^{\circ}$ , hence adsorbed molecules are expected to lose all their entropy upon adsorption [14]. Taking the standard entropy values of 1.93 and 1.35 meV/K for  $\text{CH}_4$  and  $\text{H}_2$ , respectively, the Gibbs energies for reaction steps 1 and 5 can be calculated, following Lide et al. [57], with Eq. (1.11) and are as follows:

$$\Delta G_1 = 4.725 + (0.00193 \times T) \text{ eV.} \quad (3.4)$$

$$\Delta G_5 = -4.479 - (0.00135 \times T) \text{ eV.} \quad (3.5)$$

Finally, all equilibrium constants are calculated according to Eq. (1.10) and the free surface coverage function is complete.

### 3.1.6 Activation energy

The last term that needs to be covered is the rate expression  $k_4$  which is

$$k_4 = \frac{k_B T}{h} \exp\left(\frac{-\Delta E_4^A}{k_B T}\right) \quad (3.6)$$

where  $\Delta E_4^A$  can be obtained according to Eq. (1.7) as

$$E^A = \sum_{i=1}^N \gamma_i \Delta E_i + \xi.$$

NEB calculations were carried out as described in chapter 2.3.4 to obtain  $\gamma_i$  and  $\xi$ . The potential energy diagrams of CH dissociation, once without any catalyst present and once adsorbed on a (111) fcc-Cu surface, are shown in Fig. 3.5. An impact of the Cu is clearly visible from this graph, resulting in lower activation energy. The activation energies are 4.7 eV without, and 3.41 eV with the Cu surface present. These values are used to solve Eq. (3.7), yielding

$$E_4^A = 0.268 \Delta E_{\text{Ads,C}} + 4.7 \text{ eV.}$$

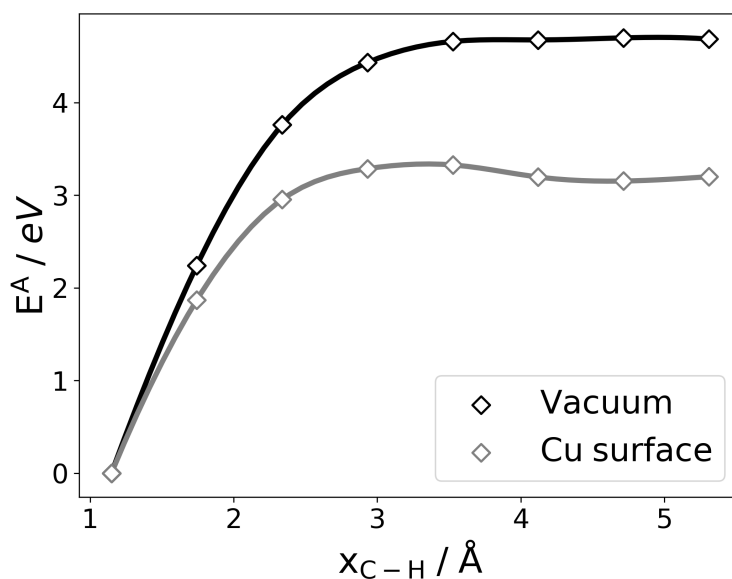


Figure 3.5: Nudged elastic band calculations for CH dissociation in vacuum (black line) and on a (111) fcc-Cu surface (grey line).

## 3.2 Reaction rate

Every term necessary to calculate  $R$  has now been derived and computed. The final step is to combine the functions into  $R$ . Since  $R = R(\Delta E_{\text{Ads,C}}, T, p)$ , appropriate input parameters for partial pressure  $p$  and temperature  $T$  need to be chosen. A first reasonable attempt is  $T=1000$  K with a partial pressure  $p_{\text{CH}_4} = 0.99$  and  $p_{\text{H}_2} = 0.01$  which would approximate the environment inside of a pyrolysis reactor at a significantly lower temperature than the operating temperature without a catalyst present, which is around 1300 K. The corresponding coverage of free sites  $\theta_*$  is shown in Fig. 3.6. At first sight, the shape of the function closely resembles the expected shape as shown in Fig. 1.1 which validates the model as well as the derivation. The surface coverage appears to be unaltered until high adsorption energies of approx.  $-7$  eV. Then, the surface occupation starts to increase rapidly within a small energy bandwidth of 1 eV. This abrupt behaviour is expected to decrease with increasing temperature due to a broader energy distribution within the gas.

The corresponding reaction rate is shown in Fig. 3.7. The maximum turnover frequency is at  $E_{\text{Ads,C}}$  values of around  $-7.5$  eV. The best performing surfaces are Rh, along with Ru, Y, Sc, Nb, and W, which are also close to the maximum. Overall, the occurrence of materials around the maximum is very high. This may be due to the fact that this energy range is densely populated when taking a look at the adsorption energy scaling relation in Fig. 3.1, and also because of the increased temperatures, which cause a slow flattening before and after the maximum. The apparent gap in energies that was already mentioned in chapter 3.1.2 appears to be a useful cutoff. Any element to the right of this gap in Fig. 3.1 results in significantly lower reaction rates and is therefore recommended to be disregarded for possible experiments with similar input parameters.

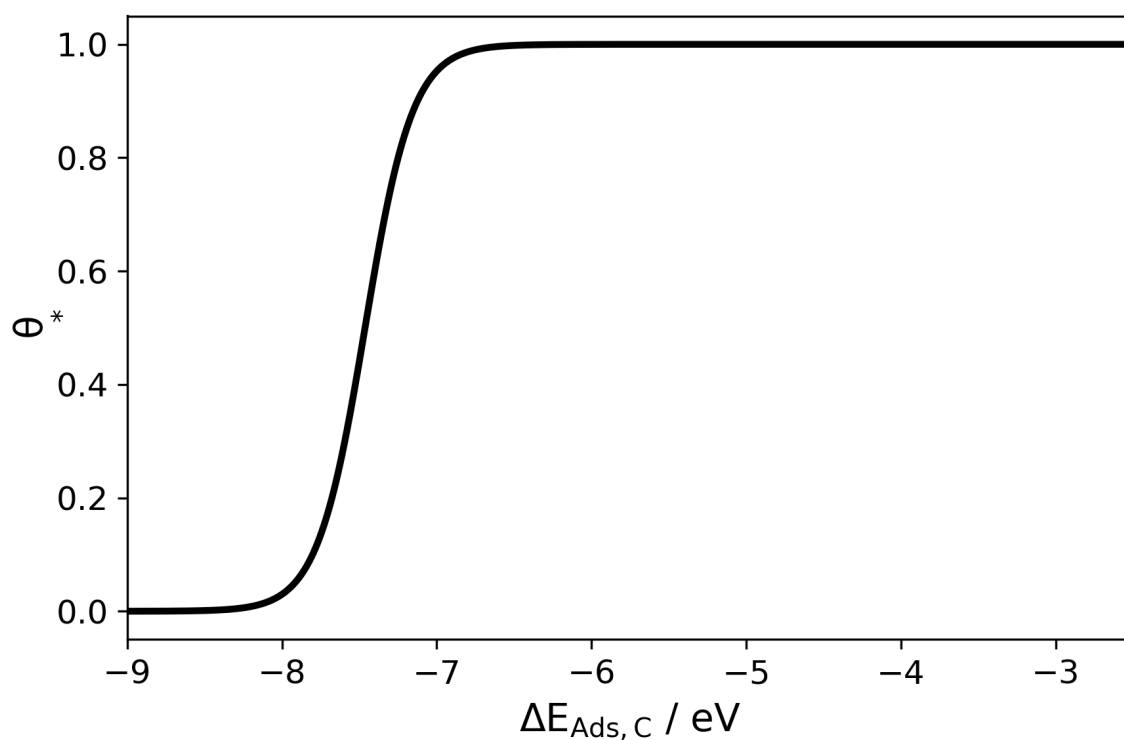


Figure 3.6: Free surface site coverage  $\theta_*$  as a function of  $E_{\text{Ads,C}}$  for  $T=1000$  K,  $p_{\text{CH}_4} = 0.99$  and  $p_{\text{H}_2} = 0.01$ .

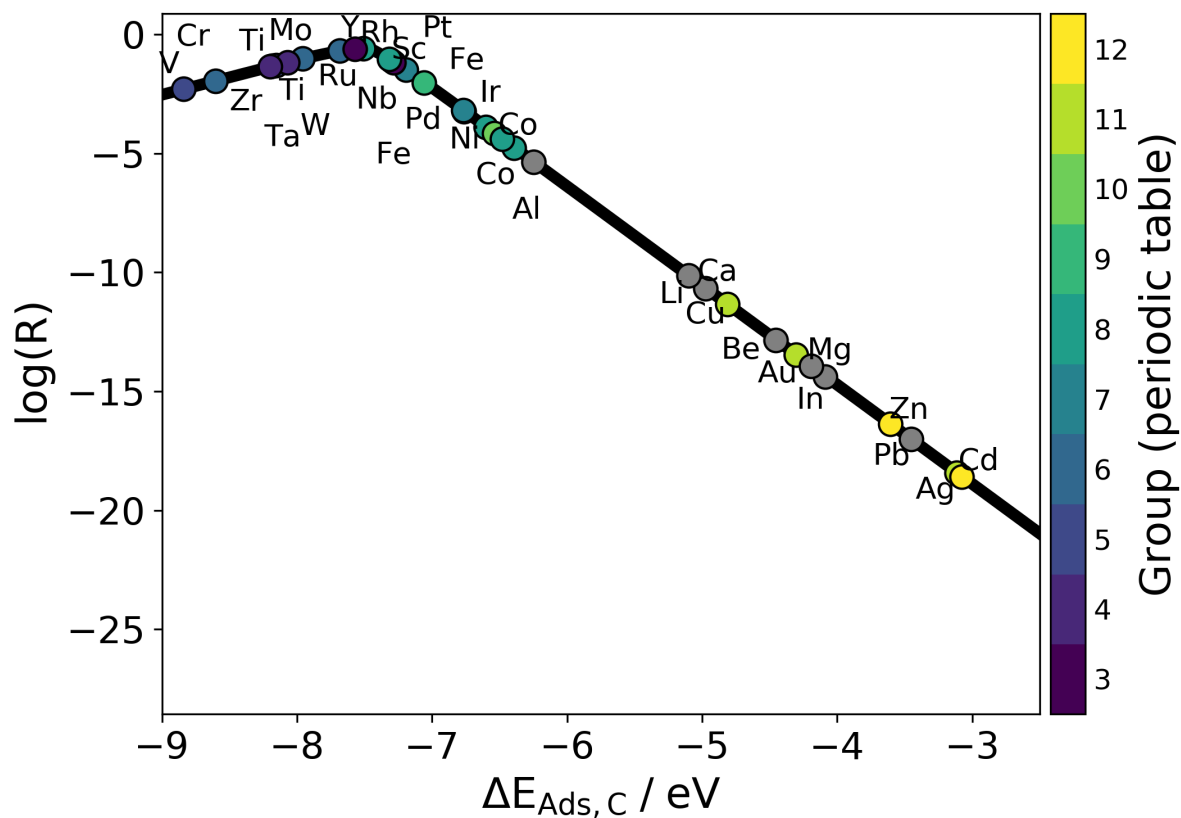


Figure 3.7:  $\log(R)$  as a function of  $E_{\text{Ads,C}}$  for  $T=1000$  K,  $p_{\text{CH}_4} = 0.99$  and  $p_{\text{H}_2} = 0.01$ .

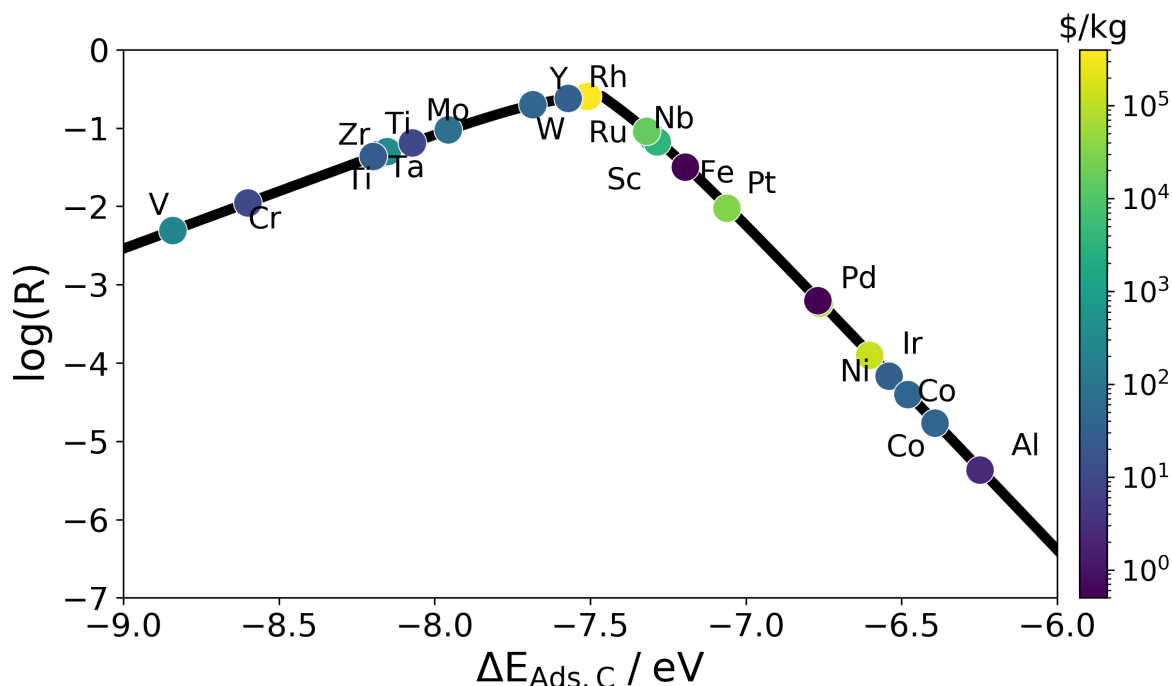


Figure 3.8: Area around the maximum  $\text{Log}(R)$  for  $T=1000$  K,  $p_{\text{CH}_4} = 0.99$  and  $p_{\text{H}_2} = 0.01$  with color-coded markers according to the logarithm of the global market price.

Since a clear correlation between the position of an element in the d-block and the adsorption energy has been shown in chapter 3.1.3, Fig. 3.7 advises against carrying out experiments with elements from group 11 and 12. However, the quantitative differences between the catalysts close to the maximum still need to be investigated experimentally.

Furthermore, other factors must also be considered when choosing a suitable catalyst. In Fig. 3.8, the elements around the maximum of Fig. 3.7 were color-coded according to their global market price as of February 2023 [58] in US Dollar (\$) per kg. The price scale is logarithmic due to the vast range in prices of considered materials between 0.5 and 400.000 \$/kg. For economic upscaling of catalytic methane pyrolysis to industrial application, a consideration of price will be of great importance. Unfortunately, by far the most expensive material, namely Rh, is closest to the maximum for the chosen conditions, hence other materials close to this maximum such as Y or W should be considered as well.

An alternative option, which is one of the most important features of this model, is to adjust pressure and temperature, thus shifting the maximum of  $R$ . In Fig. 3.9, the plot on top shows  $R$  as a function of different temperatures. The difference in reaction rates between room temperature and 1300 K is enormous, exceeding 20 orders of magnitude. A higher temperature correlates with a higher reaction rate. Moreover, the slope in  $R$  decreases with increasing temperature, indicating the mitigated role of a catalyst that is usually observed at high temperatures. Nevertheless, the catalyst still shows significant impact on the reaction behaviour.

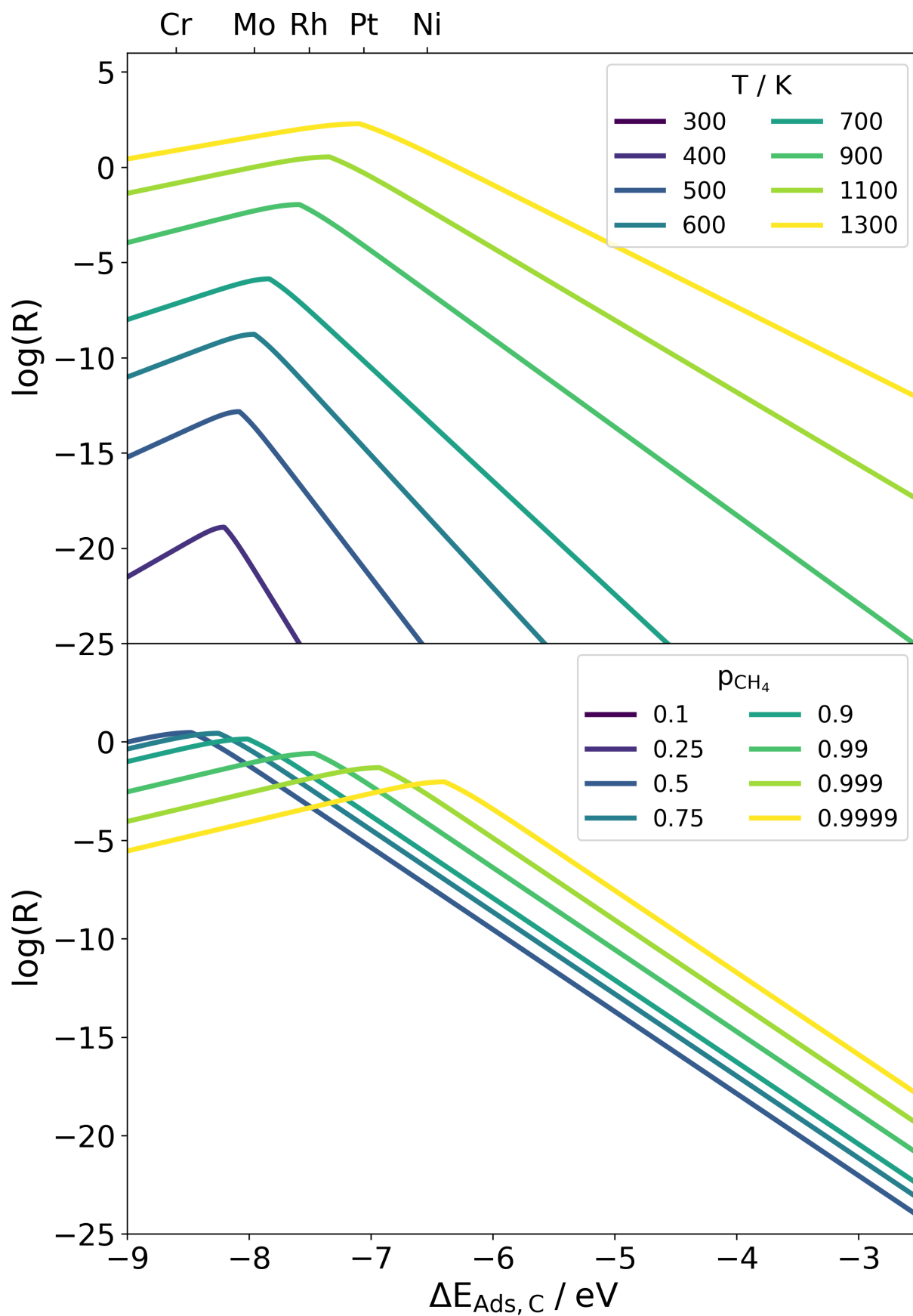


Figure 3.9: Top:  $\log(R)$  as a function of  $E_{\text{Ads,C}}$  for different temperatures ( $p_{\text{CH}_4} = 0.99$  and  $p_{\text{H}_2} = 0.01$ ). Bottom:  $\log(R)$  as a function of  $E_{\text{Ads,C}}$  for different pressures ( $T = 1000$  K).

Another interesting observation is the shift of the maximum towards adsorption energies of lower magnitude. In Fig. 3.6 it was already noted that higher temperatures will cause a movement to the right, which is highlighted by the presented graph. For instance, the maximum at 1300 K is for example in the range of Pt and Pd. Thus, it can be claimed that a catalyst can be reasonably selected only together with the desired operating temperature.

The influence of partial pressure on the overall reaction rate is less significant, as is shown in the lower graph in Fig. 3.9. However, increasing partial pressure of methane can shift adsorption energies to smaller values than temperature is capable of. Strikingly, an increasing amount of reactants present does not increase the turnover frequency. In contrary, with increasing reactant content, the reaction rate decreases slightly.

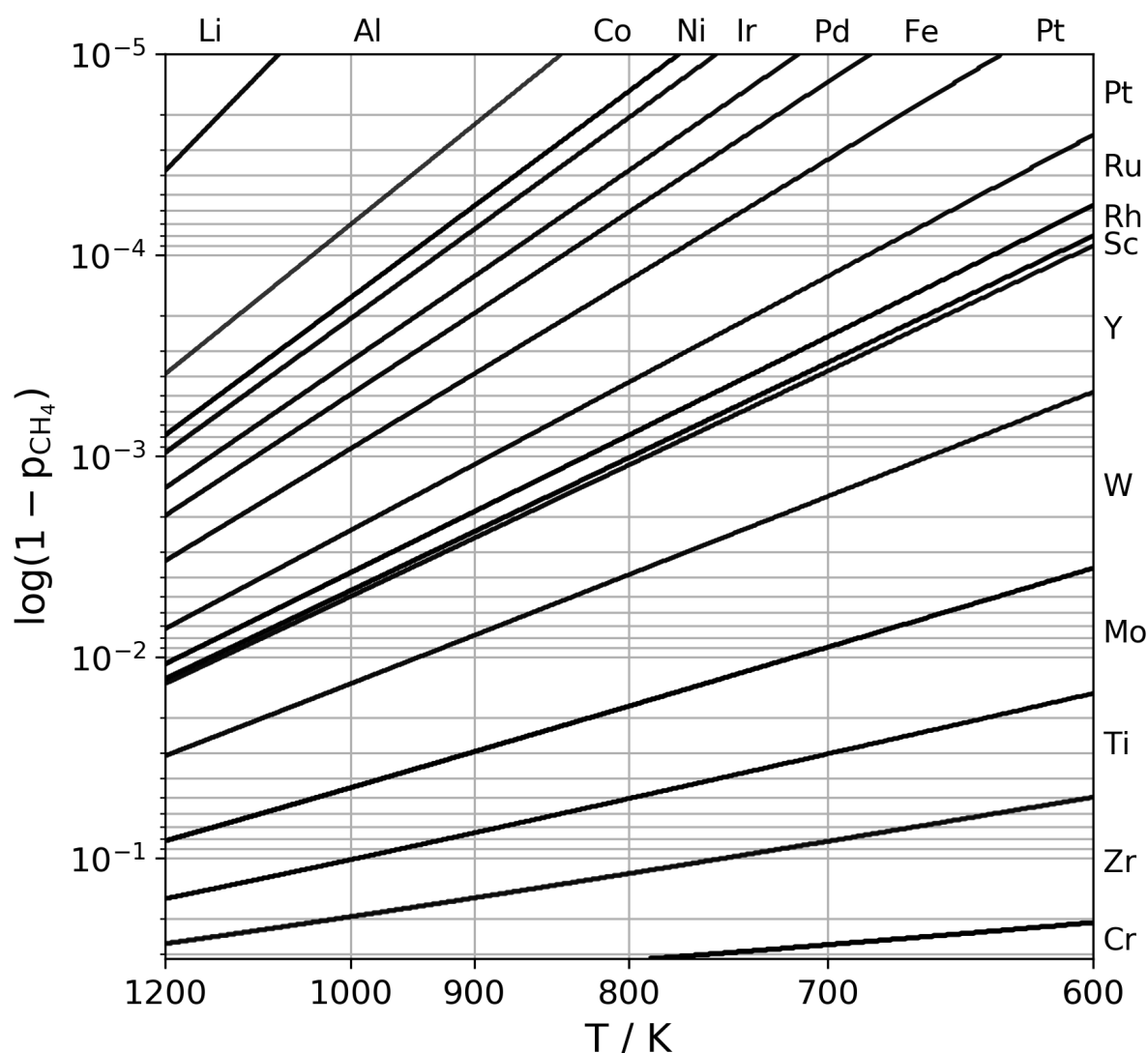


Figure 3.10: Arrhenius plot of the ideal catalyst as a function of  $T$  and  $\log(p_{\text{H}_2}) = \log(1 - p_{\text{CH}_4})$ .

The reaction rate is a function whose maximum can always be assigned to a particular catalyst material contained in the linear adsorption energy relation. Thus, the optimized reaction rate is exclusively a function of the thermodynamic conditions within the system. This feature can be utilized by plotting the optimum catalyst in the combined  $p$ - and  $T$ -space, i.e. in an Arrhenius plot, as shown in Fig. 3.10. At the edges of the diagram, the respective optimal catalysts are listed next to their phase fields.

It is clearly visible how the optimum moves towards lower adsorption energies with increasing temperature and partial pressure of  $\text{CH}_4$ , as already shown in Fig. 3.9. For very high temperature and almost pure methane atmosphere inside the reactor, the reaction rate maximum even shifts beyond the gap at  $E_{\text{Ads,C}} = -6$  eV to Li. In total, 17 different elements are closest to the maximum of  $R$  at least once for a temperature range between 600 and 1200 K and a partial pressure range of  $\text{H}_2$  between  $10^{-1}$  and  $10^{-5}$ , suggesting that the operating conditions and catalyst material should be closely matched. Hence, such a diagram could be useful for future practical purposes.

## 3.3 Limitations

For the presented model, the aim was to optimize the trade-off between computational effort and predictive power. Due to the complex nature of a multi-step catalytic chemical reaction it is obvious that a complete mathematical description of the process is considered to be impossible. In general, only the reaction path of least resistance will impact the reaction rate in a meaningful way. The key point in this task is the elimination of those factors that either have no influence on the optimal path or do not qualitatively change the result. The factors that were considered negligibly are discussed below. These remarks should also serve as suggestions for further studies.

### 3.3.1 Molecule orientation

For all calculations, the contact between hydrogen atoms and catalyst surface atoms was maximized. Preliminary studies have shown that such a setup yields more stable results which are also less dependent on the exact surface position. Fig. 3.11 shows two PES, both depicting the same section on a (001) fcc-Cu surface. Both surfaces were scanned with a  $\text{CH}_4$  molecule. For the left PES, the  $\text{CH}_4$  was orientated in a way that three H atoms were as close to the surface as possible. For the right PES, the contact between H and Cu was minimized by flipping the  $\text{CH}_4$  upside down, resulting in only one H atom interacting with the surface.

Two conclusions can be drawn from these plots. First, the resolution of the actual metal surface is much higher when scanning with maximized H-Cu interaction. Second, the energy

difference is more than an order of magnitude smaller and within a range of only 0.02 eV, making the calculation virtually independent of the initial position of the molecule as long as the adsorbate-substrate interaction is maximized. It has to be mentioned, however, that this effect is expected to decrease with a decreasing number of H atoms attached to the central C atom. Furthermore, more extensive studies on other adsorbates and substrates are still pending.

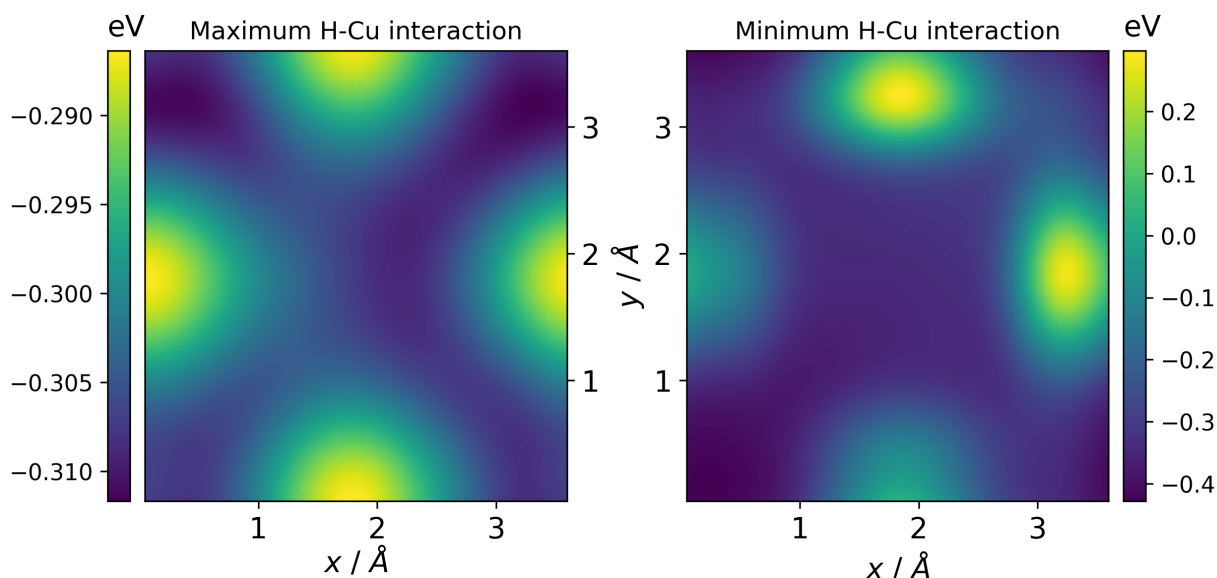


Figure 3.11: Potential energy surfaces of a (001) fcc-Cu surface scanned with a  $\text{CH}_4$  molecule. Left: Interaction between Cu surface and H atoms was maximized. Right: Interaction between Cu surface and H atoms was minimized.

### 3.3.2 Surface geometry and composition

Another important factor to consider is the assumption of a perfectly flat surface structure. Real crystals differ by having gaps, steps, or terraces, where the interaction between substrate and molecule is likely to be stronger due to closer contact. Such calculations are more complicated because the simulation cells must be much larger to minimize the effects of periodic boundary conditions, which greatly increases the computational cost. However, since the interaction is still governed by the same basic principles, the inclusion of more complex surface geometries is not expected to qualitatively change the results.

In addition, several of the materials studied, such as Zn, Pb or Al, are liquid at least over a wide range of the above operating temperatures. A liquid catalyst completely changes the kinetics of the process, therefore making it even more difficult to predict catalytic behaviour.

Alloys were not considered during this work since it would expand the configurational space to an indefinite size. Once this model is refined, machine learning could be applied to vary the surface compositions and observe any effects on scaling relationships and catalytic behaviour.



### 3.3.3 Linearity

Correlation coefficients for the performed calculations were between 0.81 and 0.94, which indicates suitable correlation. However, there are notable outliers, especially when examining the linear scaling relation between C and H. It is unclear how this will affect the validity of the result, hence significant deviations cannot be ruled out. One option for future optimization could be to refine the input parameters in the INCAR file to increase correlation of adsorption energies and thus allowing more reliable predictions. Another option is to abandon a linear model and perform a more comprehensive material study. The resulting scaling relationship can then be fitted to a nonlinear function. Such a method could also make use of current machine learning techniques.

### 3.3.4 Carbon

As already noted in chapter 1.3, carbon desorption was completely neglected during performed calculations. This simplification is necessary due to the fact that carbon forms a variety of different C structures, but also hydrocarbons such as acetylene ( $C_2H_2$ ), propylene ( $C_3H_6$ ), or benzene ( $C_6H_6$ ) among many others [59]. Due to the sheer amount of significantly more complex structures, this would also be an opportunity to apply machine learning

### 3.3.5 Entropy

Reaction entropies were only included for the adsorption and desorption reaction. It is possible to determine reaction entropies with DFT by calculating vibrational frequencies and using statistical thermodynamics, but this would have exceeded the scope of this thesis.

### 3.3.6 Rate-determining step

While CH dissociation was chosen to be the rate-determining reaction step, some studies arrived at different conclusions [29, 30]. An interesting subsequent study would be the change in reaction energy for different rate-determining steps. If the selection of only one rate-determining step is considered to be a misrepresentation of the overall reaction rate, a model derivation is significantly more complicated.

### 3.3.7 Computational accuracy

The general aim of this thesis was a workflow that is as robust and reliable as possible. Therefore, parameter optimization for most of the calculations were kept at a minimum. Detailed studies of the individual adsorbate-substrate systems could thus significantly improve accuracy and correlation.



---

## Conclusions

In this thesis, a model for the calculation of a catalyst material for methane pyrolysis was derived and presented. Relevant chemical models such as the Sabatier, transition-state and microkinetic model were introduced and applied to the methane pyrolysis reaction. Required energies were adsorption, reaction and activation, all of which were obtained from density functional theory (DFT) calculations. The resulting model computes a reaction rate that is solely a function of temperature  $T$ , partial pressures  $p_i$ , and adsorption energy scaling relations which are solely functions of the adsorption energy of carbon  $E_{\text{ads,C}}$ . The model is considered to be valid for any catalyst material that follows linear adsorption energy scaling relationships and yields a qualitative comparison of the materials.

The Vienna Ab initio Simulation Package (VASP) was used to carry out DFT calculations. Three crystal structures were considered, face-centered cubic (fcc), body-centered cubic (bcc) and hexagonal close-packed (hcp), with a total of 30 different elements included in the model.

Strong correlation was found between the adsorption energies of  $\text{CH}_n$  ( $n = 1, 2, 3$ ) and C on (111) surfaces for fcc and bcc and (0001) surfaces on hcp, with a Pearson correlation coefficient of approx. 0.9. Correlation between H and C was less pronounced at around 0.8. The model predicts Rhodium to be the best performing catalyst material at  $T = 1000$  K,  $p_{\text{CH}_4} = 0.99$  and  $p_{\text{H}_2} = 0.01$ . In addition, the model enables a search in the T-p space for an optimal catalyst material. For a temperature range between 600 and 1200 K and a partial pressure range for  $\text{H}_2$  between  $10^{-1}$  and  $10^{-5}$ , a total of 17 different materials were found to be optimal catalyst materials at least once. Performed calculations suggest that catalyst selection and reactor operating conditions should be matched.

For future studies, the established model still offers numerous optimization possibilities in terms of surface geometries, composition, the role of carbon, and the overall accuracy. It is therefore strongly recommended to incorporate current machine learning algorithms into the material screening process.



---

# Bibliography

- [1] H. Pörtner and D. Roberts, Cambridge University Press. **102** (2022).
- [2] J. Blunden and T. Boyer, Bull. Am. Meteorol. Soc. **102**, S1 (2021).
- [3] Council of European Union, “The european green deal,” (2019).
- [4] Council of European Union, “REPowerEU plan,” (2022).
- [5] “Chemistry of the elements,” (Elsevier, 1997) Chap. Hydrogen, pp. 32–67.
- [6] M. Hermesmann and T. Müller, Progress in Energy and Combustion Science **90**, 100996 (2022).
- [7] International Energy Agency., “The future of hydrogen - seizing today’s opportunities: Report prepared by the IEA for the G20.” (2019).
- [8] L. Bertuccioli and A. Chan, “Development of water electrolysis in the european union,” (Fuel Cells and Hydrogen Joint Undertaking, 2014).
- [9] R. B. Dopp, “High rate and high efficiency hydrogen generation via water electrolysis catalyzed by nano powders.” (2013).
- [10] Eurostat (European Statistical Office), “Electricity prices for non-household consumers - bi-annual data (from 2007 onwards).” (2022).
- [11] M. Katebah, M. Al-Rawashdeh, and P. Linke, Cleaner Engineering and Technology **10**, 100552 (2022).
- [12] N. Sánchez-Bastardo, R. Schlögl, and H. Ruland, Chemie Ingenieur Technik **92**, 1596 (2020).
- [13] D. C. Upham, V. Agarwal, A. Khechfe, Z. R. Snodgrass, M. J. Gordon, H. Metiu, and E. W. McFarland, Science **358**, 917 (2017).

## BIBLIOGRAPHY

---

- [14] J. K. Norskov, F. Studt, F. Abild-Pedersen, and T. Bligaard, *Fundamental concepts in heterogeneous catalysis* (John Wiley & Sons, Nashville, TN, 2014).
- [15] P. Atkins, J. de Paula, and R. Friedman, *Physical chemistry: Quanta, matter, and change*, 2nd ed. (W. H. Freeman, 2014).
- [16] G. Radnóczy and P. B. Barna, in *Materials Surface Processing by Directed Energy Techniques* (Elsevier, 2006) pp. 443–474.
- [17] H. Knözinger and K. Kochloefl, “Heterogeneous catalysis and solid catalysts,” (2003).
- [18] M. Anand, B. Rohr, M. J. Statt, and J. K. Nørskov, *The Journal of Physical Chemistry Letters* **11**, 8518 (2020).
- [19] G. Rothenberg, *Catalysis* (Wiley-VCH Verlag, Weinheim, Germany, 2008).
- [20] T. Engel and P. Reid, *Physical Chemistry*, 3rd ed. (Pearson, Upper Saddle River, NJ, 2012).
- [21] T. W. Graham Solomons and C. B. Fryhle, *Organic chemistry*, 11th ed. (John Wiley & Sons, Nashville, TN, 2012).
- [22] F. Abild-Pedersen, J. Greeley, F. Studt, J. Rossmeisl, T. R. Munter, P. G. Moses, E. Skúlason, T. Bligaard, and J. K. Nørskov, *Physical Review Letters* **99** (2007).
- [23] P. Erdi, *Mathematical models of chemical reactions* (Princeton University Press, Princeton, NJ, 1989).
- [24] J. E. McMurry, R. C. Fay, J. K. Robinson, and J. Zubricky, *Student Study Guide for Chemistry*, 7th ed. (Pearson, Upper Saddle River, NJ, 2015).
- [25] J. Moulijn, ed., *Catalysis*, Studies in surface science and catalysis (Elsevier Science, London, England, 1993).
- [26] A. H. Motagamwala and J. A. Dumesic, *Chemical Reviews* **121**, 1049 (2020).
- [27] U. Ashik, W. W. Daud, and H. F. Abbas, *Renewable and Sustainable Energy Reviews* **44**, 221 (2015).
- [28] J.-W. Snoeck, G. Froment, and M. Fowles, *Journal of Catalysis* **169**, 250 (1997).
- [29] G. Kozlov and V. Knorre, *Combustion and Flame* **6**, 253 (1962).
- [30] R. Baker, *Journal of Catalysis* **26**, 51 (1972).
- [31] S. Hofmann, G. Csányi, A. C. Ferrari, M. C. Payne, and J. Robertson, *Physical Review Letters* **95** (2005).

- 
- [32] C. Fan, Y.-A. Zhu, Y. Xu, Y. Zhou, X.-G. Zhou, and D. Chen, *The Journal of Chemical Physics* **137**, 014703 (2012).
- [33] S. Helveg, C. López-Cartes, J. Sehested, P. L. Hansen, B. S. Clausen, J. R. Rostrup-Nielsen, F. Abild-Pedersen, and J. K. Nørskov, *Nature* **427**, 426 (2004).
- [34] D. Chen, K. Christensen, E. Ochoa-Fernandez, Z. Yu, B. Totdal, N. Latorre, A. Monzon, and A. Holmen, *Journal of Catalysis* **229**, 82 (2005).
- [35] Y. B. Band and Y. Avishai, in *Quantum Mechanics with Applications to Nanotechnology and Information Science* (Elsevier, 2013) pp. 871–889.
- [36] W. Kohn, *Rev. Mod. Phys.* **71**, 1253 (1999).
- [37] P. Hohenberg and W. Kohn, *Physical Review* **136**, B864 (1964).
- [38] W. Kohn and L. J. Sham, *Physical Review* **140**, A1133 (1965).
- [39] S. Müller, *Journal of Physics: Condensed Matter* **15**, R1429 (2003).
- [40] T. Tsuneda, *Density Functional Theory in Quantum Chemistry* (Springer Japan, 2014).
- [41] G. Kresse and J. Hafner, *Physical Review B* **48**, 13115 (1993).
- [42] E. R. Davidson, *Journal of Computational Physics* **17**, 87 (1975).
- [43] D. M. Wood and A. Zunger, *Journal of Physics A: Mathematical and General* **18**, 1343 (1985).
- [44] J. P. Perdew, K. Burke, and M. Ernzerhof, *Physical Review Letters* **77**, 3865 (1996).
- [45] B. Hammer, L. B. Hansen, and J. K. Nørskov, *Physical Review B* **59**, 7413 (1999).
- [46] P. E. Blöchl, *Physical Review B* **50**, 17953 (1994).
- [47] M. K. Horton, J. H. Montoya, M. Liu, and K. A. Persson, *npj Computational Materials* **5** (2019).
- [48] A. Jain, S. P. Ong, G. Hautier, W. Chen, W. D. Richards, S. Dacek, S. Cholia, D. Gunter, D. Skinner, G. Ceder, and K. A. Persson, *APL Materials* **1**, 011002 (2013).
- [49] G.-F. Chen, Y. Yuan, H. Jiang, S.-Y. Ren, L.-X. Ding, L. Ma, T. Wu, J. Lu, and H. Wang, *Nature Energy* **5**, 605 (2020).
- [50] H. Jónsson, G. Mills, and K. W. Jacobsen, in *Classical and Quantum Dynamics in Condensed Phase Simulations* (World Scientific, 1998).

## BIBLIOGRAPHY

---

- [51] H. Partridge and C. W. Bauschlicher, *The Journal of Chemical Physics* **103**, 10589 (1995).
- [52] S. J. Blanksby and G. B. Ellison, *Accounts of Chemical Research* **36**, 255 (2003).
- [53] S.-W. Kim, J.-H. Lee, H.-J. Kim, and J.-H. Cho, *Chemical Physics Letters* **557**, 159 (2013).
- [54] S. Siekierski and J. Burgess, in *Concise Chemistry of the Elements* (Elsevier, 2002) pp. 131–154.
- [55] R. J. Deeth, in *Advances in Inorganic Chemistry* (Elsevier, 2010) pp. 1–39.
- [56] PubChem, “Periodic table of elements,” <https://pubchem.ncbi.nlm.nih.gov/periodic-table/>., accessed: 2023-1-10.
- [57] D. R. Lide, *CRC handbook of chemistry and physics, 84th edition*, 84th ed. (CRC Press, Boca Raton, FL, 2003).
- [58] S. M. Market, “Shanghai metals market (SMM),” (2023).
- [59] H. Ogihara, H. Tajima, and H. Kurokawa, *Reaction Chemistry & Engineering* **5**, 145 (2020).